MEDICAL ROBOTS

Photocatalytic microrobots for treating bacterial infections deep within sinuses

Haidong Yu[1,2]†, Xurui Liu[3]†, Yabin Zhang[1]*, Jie Shen[4], Xijun Liu[1], Shubo Liu[4], Xiangyu Wang[1], Bonan Sun[3], Huihui Du[3], Lin Xu[5], Bingsuo Zou[1], Jianning Ding[6], Qingsong Xu[7], Li Zhang[3]*, Ben Wang[2]*

Microrobotic techniques are promising for treating biofilm infections located deep within the human body. However, the presence of highly viscous pus presents a formidable biological barrier, severely restricting targeted and minimally invasive treatments. In addition, conventional antibacterial agents exhibit limited payload integration with microrobotic systems, further compromising therapeutic efficiency. In this study, we propose a photocatalytic microrobot through a magnetically guided, optical fiber–assisted therapeutic platform specifically designed to treat bacterial infections in deep mucosal cavities. The microrobots comprising copper (Cu) single atom–doped bismuth oxoiodide (BiOI), termed CBMRs, can be guided and tracked by real-time x-ray imaging. Under external magnetic actuation, the illuminated region from the magnetically guided optical fiber synchronously follows the CBMR swarm, enabling effective antibacterial action at targeted infection sites. Upon continuous visible-light irradiation, the resultant photothermal effect substantially reduces the viscosity of pus on inflamed mucosal tissues, enhancing the penetration capability of the CBMR swarm by more than threefold compared with baseline conditions. Concurrently, atomic-level design of CBMRs facilitates robust generation of reactive oxygen species, enabling efficient biofilm disruption and reductions in bacterial viability. We validated the effectiveness of this integrated optical fiber–assisted microrobotic platform in a rabbit sinusitis model in vivo, demonstrating its potential for clinically relevant infection therapy.

INTRODUCTION

Biofilms, which can occur in various organs in humans, are complex microbial communities formed by multiple microorganisms attached to a surface (*1*). Once aggregated, such microorganisms produce and secrete extracellular polymeric substances (EPS) that form a three-dimensional (3D) physical scaffold, maintaining the organized structure of the microbial community (*2*). This stable architecture provides efficient protection against external interferences, particularly mechanical agitation and antibiotics (*3*). Therefore, the biofilm is difficult to eliminate, affecting the physiology and health of the host and even leading to host death. The formed biofilm on the human body often triggers severe inflammatory responses, accompanied by the formation of biological barriers from the shedding of in situ cells and deposition of highly viscous pus-like secretions after immune cell death. These barriers further shield internal biofilms from conventional treatments, especially within deep cavities where inflammatory responses occur, particularly in the respiratory system, digestive system, and ear canal. As a prevalent respiratory condition, sinusitis is closely linked to biofilm infections caused by *Streptococcus pyogenes*, which contribute to disease persistence and treatment resistance. Clinically, this bacterial-induced inflammation affects the sinus mucosa, characterized by symptoms such as nasal congestion, thick purulent nasal discharge, reduced sense of smell, facial pain, and occasionally severe memory impairment (*4*). Epidemiological studies indicate that the global prevalence of chronic rhinosinusitis ranges from ~8 to 13%, varying by region (*5*). Moreover, sinusitis easily reoccurs because of the narrow and imperceptible entrance size (2 to 3 mm) as well as the presence of a biological barrier formed by abundant inflammatory secretions on the lining that substantially hampers treatment efficacy (*6*). Current clinical treatments for sinusitis primarily include antibiotic administration, nasal irrigation, and maxillary sinus puncture irrigation (*7*). However, extensive antibiotic use has led to antimicrobial resistance, and invasive procedures often cause nasal discomfort and irreversible tissue damage. To address these limitations, existing research on treating bacterial infections in deep microcavities mainly involves passive drug delivery via blood circulation, which lacks effective localized targeting strategies. Unfortunately, such passive methods typically result in low therapeutic efficiency and may impose additional burden on renal function (*8*). Therefore, there is a clinical need for an effective, minimally invasive strategy capable of actively targeting and removing bacterial biofilms within confined spaces and across high-viscosity biological barriers.

Magnetic micro- or nanorobots provide distinct advantages for antibacterial applications, including precise delivery and rapid accumulation of antibacterial agents at infection sites, thus minimizing toxic effects on healthy tissues (*9*). In addition, their collective motion generates fluid-stirring effects, promoting effective interactions between antibacterial agents and bacteria (*8*). Moreover, swarming microrobots exert mechanical shear forces under magnetic fields, effectively disrupting and disintegrating bacterial biofilms (*10*, *11*). However, effectively eradicating biofilm infections

[1]School of Chemistry and Chemical Engineering, State Key Laboratory of Featured Metal Materials and Life-cycle Safety for Composite Structures, School of Resources, Environment and Materials, Guangxi University, Nanning 530004, P. R. China. [2]College of Chemistry and Environmental Engineering, Shenzhen University, Shenzhen 518055, P. R. China. [3]Department of Mechanical and Automation Engineering, Chinese University of Hong Kong, Hong Kong, P. R. China. [4]Shenzhen Key Laboratory of Spine Surgery, Department of Spine Surgery, Peking University Shenzhen Hospital, Shenzhen 518036, P. R. China. [5]College of Mechanical Engineering, Jiangsu University, Zhenjiang, Jiangsu 212013, P. R. China. [6]School of Mechanical Engineering, Yangzhou University, Yangzhou 225009, P. R. China. [7]Department of Electromechanical Engineering, Faculty of Science and Technology, University of Macau, Taipa, Macau, P. R. China.
*Corresponding author. Email: ybzhang@gxu.edu.cn (Y.Z.); lizhang@cuhk.edu.hk (L.Z.); benwang@szu.edu.cn (B.W.)
†These authors contributed equally to this work.

on the sinus mucosa using microrobotic techniques remains challenging because of biological barriers and the limited efficacy of current antibacterial agents. In practical infection scenarios, highly viscous pus, composed primarily of dead white blood cells and bacterial debris, severely hinders microrobot mobility and reduces therapeutic efficacy (*12*). Although numerous strategies have been proposed to overcome such biological barriers (*13*–*19*), most methods focus exclusively on optimizing microrobot properties through surface modifications to minimize mucus adhesion. Unfortunately, the surface modifications frequently compromise the intrinsic catalytic activity and multifunctionality of microrobots (table S1) without effectively altering the viscosity of the biological environment itself. Therefore, it is crucial to develop comprehensive therapeutic strategies that not only optimize microrobot design but also actively modulate the surrounding microenvironment, specifically targeting mucus viscosity reduction. Such combined environmental and robotic interventions would enhance microrobot penetration and thus strengthen the overall effectiveness of biofilm eradication.

Antibacterial agents also play a pivotal role in achieving the complete eradication of biofilms. Although antibiotics have been extensively used to manage bacterial infections, their cumulative use not only presents a potential threat to global health security (*20*) but also exacerbates the antibiotic resistance of bacteria, thereby impairing therapeutic effectiveness (*21*). In contrast with antibiotics, reactive oxygen species (ROS) present distinct advantages, whose use can effectively circumvent the occurrence of antibiotic resistance and alleviate the burden on the liver organs. Such antimicrobials are usually generated from catalysts, nanozymes, and persulfate. Catalysts based on single atoms have demonstrated potential in ROS generation for antimicrobial applications (*22*). Such single-atom catalysts at the atomic level not only can enhance the atomic utilization rate, thereby augmenting the catalytic activity, but also minimize the harm caused by the release of metal ions. Compared with natural enzymes, single-atom catalysts both catalyze the production of ROS and exhibit reliable stability. They can operate efficiently in environments with a broad range of temperature and pH conditions (*23*). For instance, Fan *et al.* (*24*) substantially enhanced the efficiency of catalyzing the reaction between H_2O_2 and glucose to produce ROS using the glucose oxidase-peroxidase mimics obtained through the combination of copper single atoms and gold nanoparticles, thereby facilitating the antibacterial process. Accordingly, it is anticipated that endowing microrobots with single-atom technology, in conjunction with an enhanced capacity to penetrate biological barriers, will effectively expedite the rapid treatment of inflammatory responses induced by bacterial infections in the deep cavities of the human body.

In this study, we introduce a strategy using photocatalytic microrobots to effectively eradicate biofilm infections on the sinus mucosa (Movie 1 and Fig. 1A). Specifically, Cu single atom–loaded bismuth oxoiodide (BiOI) photocatalytic microrobots (CBMRs) were delivered into the sinus cavity through a magnetically navigable optical fiber (Fig. 1B). Visible light transmitted via the fiber activated a photothermal effect in CBMRs, facilitating their targeted localization onto inflamed mucosal surfaces. The synergistic action of abundant ROS, generated through Cu single atom photocatalysis, and mechanical disruption induced by the collective magnetic movement of a microrobot swarm enabled efficient biofilm eradication. After treatment, the restored ciliary function naturally expelled CBMRs from the nasal cavity (Fig. 1C). To achieve this therapeutic approach, we first synthesized and chemically decorated a Janus-structured magnetic BiOI with Cu single atoms, forming magnetically driven CBMRs. A magnetically controlled optical fiber was subsequently developed, ensuring precise and synchronized linkage with the microrobot swarm. Under magnetic guidance, the focused illumination from the fiber enhanced ROS generation and simultaneously induced photothermal effects, reducing the

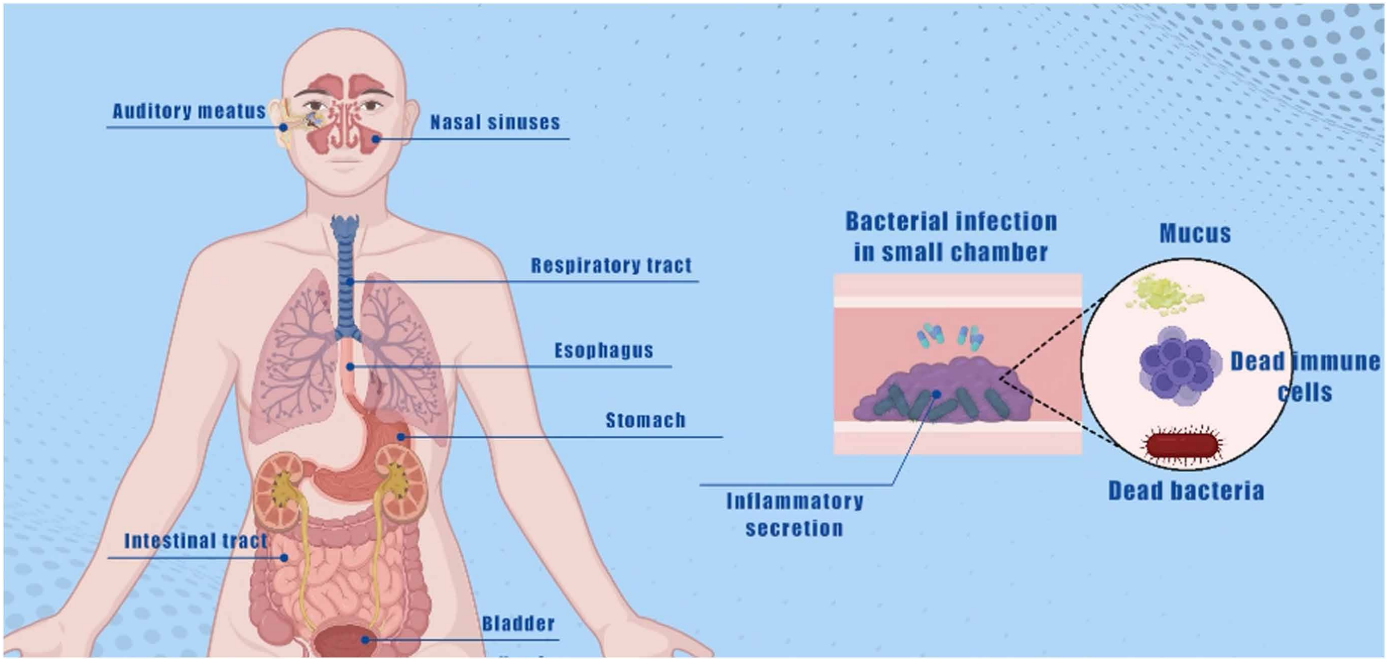

Movie 1. Overview of photocatalytic microrobots for treating bacterial infections deep within sinuses.

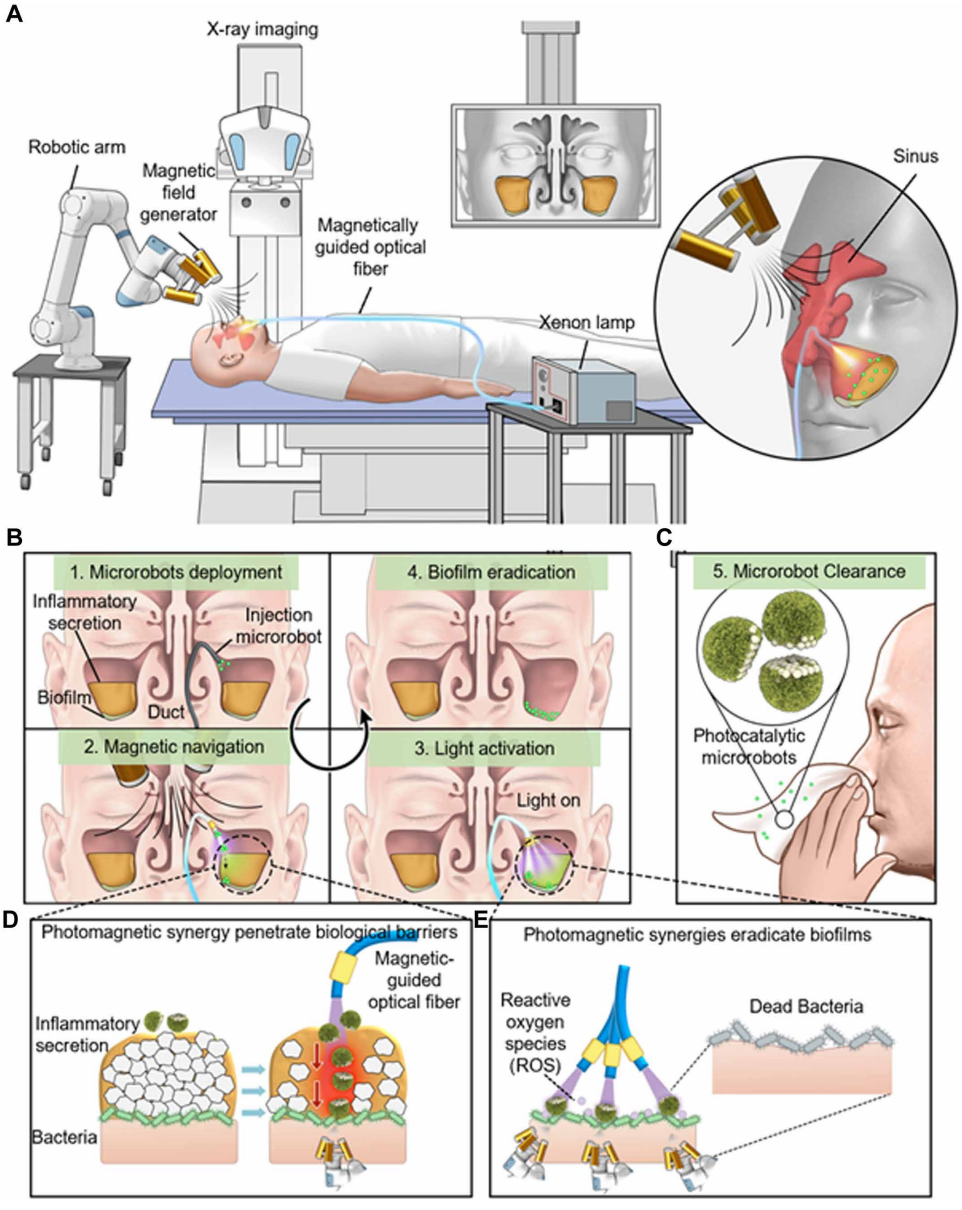

Fig. 1. Conceptual illustration of an optomagnetic collaborative therapeutic platform for biofilm eradication inside the sinus based on CBMRs. (**A**) Schematic of the overall setup, demonstrating the magnetically guided optical fiber system integrated with x-ray imaging to deploy photocatalytic microrobots for precise treatment within the sinus cavity. (**B**) Stepwise depiction of microrobot therapy, including microrobot deployment, magnetic navigation, localized activation via fiber-transmitted visible light, and subsequent biofilm eradication. (**C**) Natural clearance of microrobots by the restored ciliary action after successful treatment. (**D**) Illustration of photomagnetic synergy facilitating microrobot penetration through highly viscous inflammatory secretion barriers. (**E**) Mechanism highlighting the collaborative photomagnetic-induced generation of ROS for efficient eradication of bacterial biofilms.

viscosity of inflammatory secretions (Fig. 1, D and E). This combined photothermal-magnetic mechanism, together with mechanical shear forces, substantially improved CBMR penetration through biological barriers, facilitating rapid biofilm removal from mucosal surfaces. Unlike conventional microrobots, which typically require hydrophobic surface modifications to reduce friction during barrier penetration, our CBMR design maintains maximal catalytic activity without additional surface alterations. Using x-ray positioning and digital radiography (DR) imaging, we successfully demonstrated complete sinus function recovery in a rabbit sinusitis model through visible-light catalytic therapy via optical fiber. This approach is particularly advantageous for treating infections within narrow and complex anatomical spaces, offering a promising, minimally invasive therapeutic strategy for clinical sinusitis management and paving the way for broader in vivo applications of cooperative microrobotic therapies.

RESULTS

Fabrication and characterization of CBMRs

In conjunction with a rational system design scheme, microrobot-based therapy presents an optimal approach for achieving rapid eradication of sinus biofilms; however, this poses a challenge regarding the antimicrobial activity and robust mechanical forces exhibited by microrobots. We designed a magnetic photocatalytic microrobot loaded with Cu single atoms. The robot preparation process is shown in Fig. 2A. The Fe_3O_4@BiOI (BMRs) robot with Janus structure is prepared by the solvothermal method, where magnetic particles are deposited onto a slide surface and subsequently undergo solvothermal self-growth combined with spray coating. Furthermore, the wet-chemical method is used to dope Cu single atoms to obtain CBMRs. The microrobots integrated with photocatalytic capability and Cu single atoms have antibacterial activity. Scanning electron microscope (SEM) images (Fig. 2B and fig. S1) shows that the microrobot has a hemispherical core-shell structure with a size of about 3 μm. Fe_3O_4 is deposited at the bottom of the hemisphere as a magnetic core, and BiOI nanosheets self-assemble to form a hemisphere on the surface of Fe_3O_4, providing a photocatalytic shell. The contents of each element in CBMRs are determined as shown in table S2. The x-ray diffraction pattern (fig. S2A) shows tetragonal BiOI and cubic-phase Fe_3O_4 diffraction peaks, whereas the diffraction peaks of Cu and CuO are not found because Cu exists in the form of a single atom. The morphology and structure of the synthesized microrobot were confirmed, but no monatomic state of Cu was observed in transmission electron microscopy, as depicted in fig. S2B.

According to the nitrogen adsorption-desorption isotherms (fig. S3), the specific surface area of CBMRs is 49.1 m^2/g, which is higher than that of pure BiOI, and it can accommodate more reaction sites for ROS

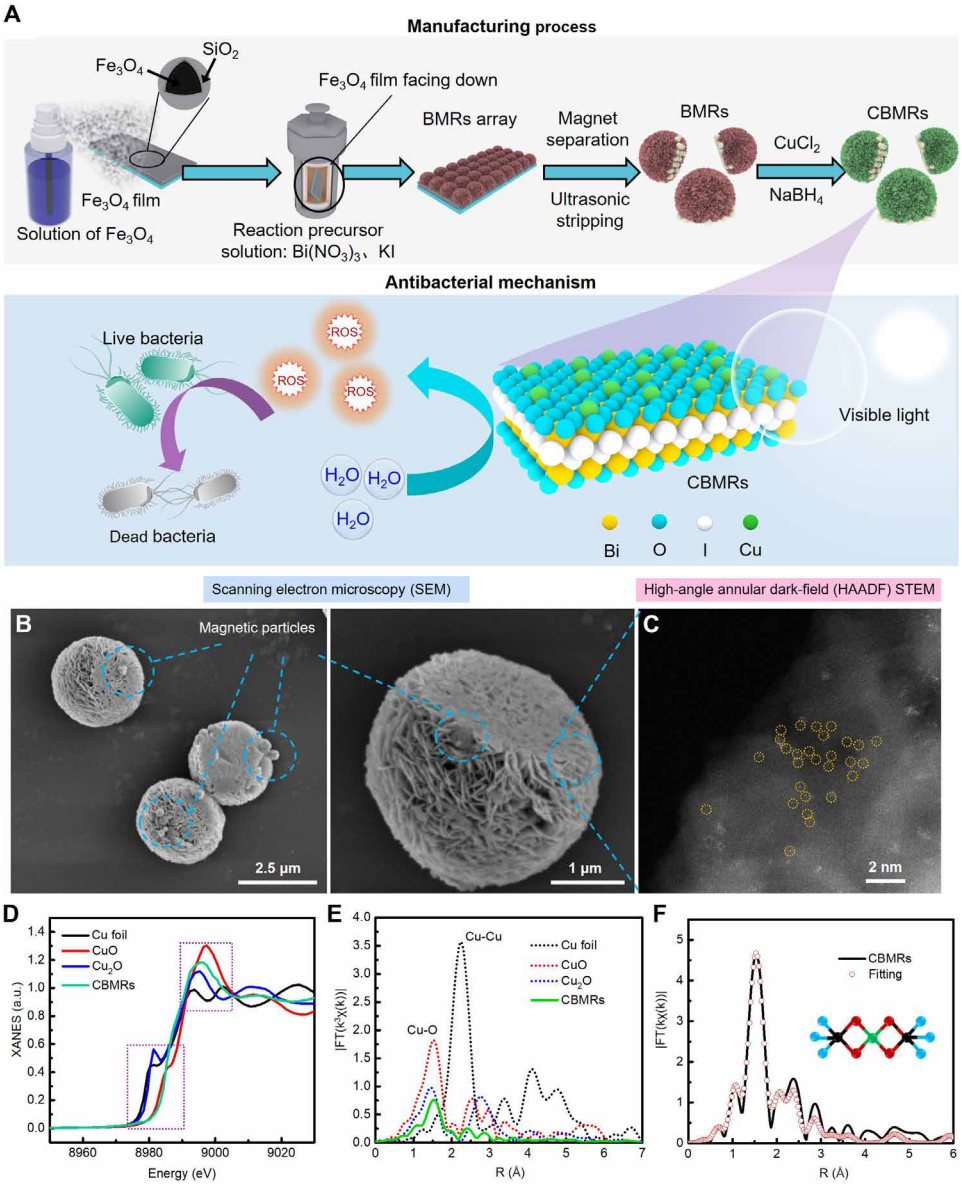

Fig. 2. Preparation and characterization of CBMRs. (**A**) Schematic illustrating the fabrication procedure of CBMRs and their antibacterial mechanism involving ROS generation under visible light. (**B**) SEM images showing the morphology of CBMRs. Magnetic Fe_3O_4 particles embedded within the microrobots are highlighted by blue circles. Scale bars, 2.5 and 1 μm. (**C**) High-angle annular dark-field scanning transmission electron microscopy (HAADF-STEM) image identifying Cu single atoms dispersed on the CBMR surface (marked by yellow circles). Scale bar, 2 nm. (**D**) XANES spectra and (**E**) EXAFS spectra at the Cu K-edge of CBMRs compared with reference samples (Cu foil, CuO, and Cu_2O). a.u., arbitrary units. (**F**) EXAFS fitting analysis of CBMRs in R-space, demonstrating the atomic coordination environment around Cu single atoms.

generation. The zeta potential measurements (fig. S4) show that CBMRs have a small amount of negative charge. X-ray photoelectron spectroscopy (XPS) analysis (fig. S5) of the Bi 4f region shows peaks at 161.08 and 166.33 eV, corresponding to Bi $4f_{7/2}$ and Bi $4f_{5/2}$, respectively. The Bi $4f_{7/2}$ peak corresponds to the oxidation state of Bi^{3+} (*25*). In addition, peaks at 932.48 and 942.38 eV observed in the Cu 2p region correspond to Cu $2p_{3/2}$ and Cu $2p_{1/2}$, respectively, indicating the coexistence of Cu^+ and Cu^{2+} (*26*, *27*). There is no evidence to indicate that copper exists in the zero-valence state. This finding further corroborates that copper does not occur in the form of a pure substance, such as clusters or nanoparticles. To verify this, an aberration-corrected TEM image of CBMRs with atomic resolution is shown in Fig. 2C. Isolated copper atoms were well dispersed on the BiOI matrix, and no obvious copper particles or clusters were found. To further investigate the state of Cu atoms, we measured the x-ray absorption energy near-edge structure (XANES) of Cu foils, Cu_2O, CuO, and CBMRs (Fig. 2D). The results show that the XANES of CBMRs are located between Cu_2O and CuO, indicating that the single valence of copper is between +1 and + 2 (*28*). Subsequently, the coordination configuration of Cu sites was analyzed by extended x-ray absorption fine structure (EXAFS). As shown in Fig. 2E, the first coordination shell is located at 1.5 Å, indicating Cu-O coordination. Meanwhile, CBMRs show no obvious Cu-Cu scattering at 2.2 Å. These results indicate the properties of isolated Cu atoms dispersed on the supporter. In addition, a wavelet transformation was performed on the basis of the EXAFS results to distinguish the backscattered atoms (fig. S6A). We observed that the maximum strengths of Cu foil, CuO, and Cu_2O were 9.7, 9.1, and 11.5 Å, respectively, which can be attributed to the Cu-Cu structure. In contrast, CBMRs show a maximum strength at 5.8 Å, assigned to the Cu-O configuration on the basis of previous reports. According to a previous study (*29*), applying the backscattering path of O, we determined that the coordination number of Cu-O is very close to 4. Meanwhile, according to the fitting results of EXAFS, the local structure of Cu atoms in CBMRs conforms to the Cu-O_4 model, and the best fit is obtained when the Cu center is coordinated with four O atoms (Fig. 2F and fig. S6B). Accordingly, the atomic Cu structure model of CBMRs can be derived, as shown in the illustration of Fig. 2F.

The above results demonstrate that we have successfully prepared CBMRs. A vibrating sample magnetometer (VSM) quantitatively detected the magnetism of the prepared CBMRs, as shown in the red curve in fig. S7A. CBMRs also have strong light absorption in the entire visible region (fig. S7B). Combined with their high specific surface area, CBMRs can produce many ROS for antibacterial applications. These results further indicate that Cu single atom–loaded magnetic BiOI microrobots have been successfully achieved, which have good application potential in terms of antibacterial activity under visible light. Combined with magnetic actuation, CBMRs are expected to achieve effective treatment of biofilms.

Magnetically guided optical fiber–integrated therapeutic platform

The photocatalytic properties of CBMRs and the synergistic interaction of Cu single atoms give rise to the production of ROS, which is crucial for antibacterial activity. Therefore, it is imperative to establish an optomagnetic cooperative platform that enables coordinated movement between microrobots and light sources. Specifically, this platform should provide navigational control over CBMRs, whereas the illumination of nearby light sources should be precisely regulated to facilitate continuous ROS generation.

First, the motion performance of CBMRs under the magnetic field was studied. The motion capability of individual CBMRs in a pure aqueous medium was evaluated within a rotating magnetic field (fig. S8). Under a 10-mT magnetic field, the velocity of CBMR reached its peak at a 7-Hz rotation frequency, exhibiting a maximum speed of 19.6 μm/s. However, because of the frequency step-out effect, a further increase in frequency leads to a decrease in speed. When maintaining a fixed frequency of 7 Hz, the motion velocity of CBMRs gradually increased with an escalation in magnetic field intensity and eventually plateaued at 10 mT, with a maximum velocity recorded at 24.3 μm/s.

Under specific parameters comprising a magnetic field intensity of 10 mT and frequency set at 7 Hz, a single CBMR demonstrated precise trajectory control along the S, Z, and U paths, highlighting its exceptional motion manipulation capabilities. However, the biofilm is a 3D stable structure, where the existence of EPS on its surface endows it with high mechanical strength, thereby making it difficult for a single microrobot to destroy the biofilm through the movement of a single microrobot. The swarming motion of magnetically driven microrobots has proven to be an effective means for the destruction of biofilms. Hence, it is of great importance to study the swarming motion performance of magnetic microrobots for the removal of biofilms. The magnetic microrobot swarm is formed within a gradient rotating magnetic field. Upon activation of the magnetic field, the micromachines align themselves into a rotating chain of particles because of the attractive magnetic dipole forces. Simultaneously, fluid interactions between these chains result in particle aggregation, gradually forming a densely populated swarm region (fig. S9A). When the rotation axis of the magnetic field is perpendicular to the base plane, the self-assembled magnetic microrobot swarm can synchronously rotate along the magnetization direction to the rotating magnetic field (*30*). To induce swarming movement, a slight tilting of the rotation plane is required to increase the component vector of the *z* axis–directed magnetic field and generate tangential friction between the microrobot swarm and the substrate. This friction serves as a driving force for directing the movement of this tiny robot swarm (*31*). Further enhancement in control systems enables omnidirectional mobility of this robotic swarm. The inclined magnetic field plane can be achieved through coordinate system transformation (Eq. 2)

$$\mathbf{B_{uvw}} = \mathbf{R}\mathbf{B_{xyz}} \tag{1}$$

$$\mathbf{R} = \begin{bmatrix} \mathbf{i_u} \times \mathbf{i_x} & \mathbf{i_u} \times \mathbf{j_y} & \mathbf{i_u} \times \mathbf{k_z} \\ \mathbf{j_v} \times \mathbf{i_x} & \mathbf{j_v} \times \mathbf{j_y} & \mathbf{j_v} \times \mathbf{k_z} \\ \mathbf{k_w} \times \mathbf{i_x} & \mathbf{k_w} \times \mathbf{j_y} & \mathbf{k_w} \times \mathbf{k_z} \end{bmatrix} \tag{2}$$

where $\mathbf{B_{uvw}}$ is the inclined magnetic field; $\mathbf{B_{xyz}}$ is the primary magnetic field; **R** is the rotation matrix; **u**, **v**, and **w** are the directions of the coordinate axes during magnetic field rotation; and **x**, **y**, and **z** correspond to the initial coordinate axis orientations. **i**, **j**, and **k** are the unit vectors in the positive direction (*32*). The schematic diagram of the magnetic field is shown in Fig. 3A, and the specific expression of the magnetic field is provided in eqs. S1 to S3. In addition, this vortex swarm enhances the mechanical force of the microrobot, and using the friction generated by the microrobot swarm presents a promising strategy for addressing biofilm issues. An in-depth investigation into the locomotion characteristics of microrobot collectives is pivotal for achieving optimal biofilm eradication efficacy.

The motion of the swarm generated by CBMRs was assessed in a rotating magnetic field produced by a permanent magnet. At a magnetic field strength of 4.7 mT, CBMRs assembled into linear particle chains, and upon increasing the field to 18.9 mT, coordinated swarming behavior was observed. CBMRs formed a synchronized swarm of circular microrobots with an approximate area of 10 mm^2 that rotated along with the permanent magnet. With a further increase in the magnetic field intensity to 45.9 mT, the swarm area expanded to 28 mm^2 and exhibited highly synchronous rotation with the permanent magnet (fig. S9B). However, when the magnetic field reached 109.5 mT, excessive magnetic force compressed the swarm tightly at its base, preventing rotational movement.

Figure 3B illustrates how different frequencies and strengths of the magnetic field influence the formation rate of CBMR swarms. In low-intensity fields (4.7 to 18.9 mT), variations in rotational frequency have a notable influence on the swarm formation rate. A higher frequency accelerates fluid interaction because of rapid particle chain rotation. At a higher intensity of 45.9 mT, swarms can form within just 20 s; further increasing intensity does not enhance their formation speed. Therefore, for achieving highly controllable CBMR swarms, selecting a magnetic field strength of 45.9 mT is most appropriate for verifying their motion characteristics. Given the requirement for sufficient mechanical force, the shape of a moving swarm will influence its controllability and mechanical force to disrupt biofilms. It is observed in Fig. 3C that low movement speeds had no obvious effect on the swarm shape. At a magnet speed of 120 μm/s, the tailing behavior of the microrobot swarm emerged under low-frequency actuation, whereas it was suppressed at higher frequencies. At speeds up to 180 μm/s, the swarm failed to maintain its complete shape at low frequencies, thereby losing its functionality for biofilm destruction. These findings highlight that the optimal magnetic field condition for the CBMRs swarm was determined to be 45.9 mT and 7 Hz, with a recommended movement speed below 150 μm/s. Using the above conditions, the microrobot swarm was successfully controlled by rotating magnets through a 3D-printed maze (fig. S10), demonstrating the controllability and excellent motion performance of magnetically driven CBMRs (movie S1).

To quantify the minute forces generated by the swarm for the destruction of biofilms, we used electrical signals obtained from piezoelectric thin film coupled amplifiers to evaluate the mechanical disruptive capability of the swarm (Fig. 3, D and E, and fig. S11, A and B). At a magnetic field strength of 45.9 mT and a frequency of 6 Hz, the swarm generates a force of up to 629 μN, which exceeds the force required for the destruction of EPS (*33*), enabling rapid biofilm eradication. When the magnetic field strength reaches 109.5 mT, a decline in the detected pressure signal is observed because of the pronounced magnetic force that has compressed the particles

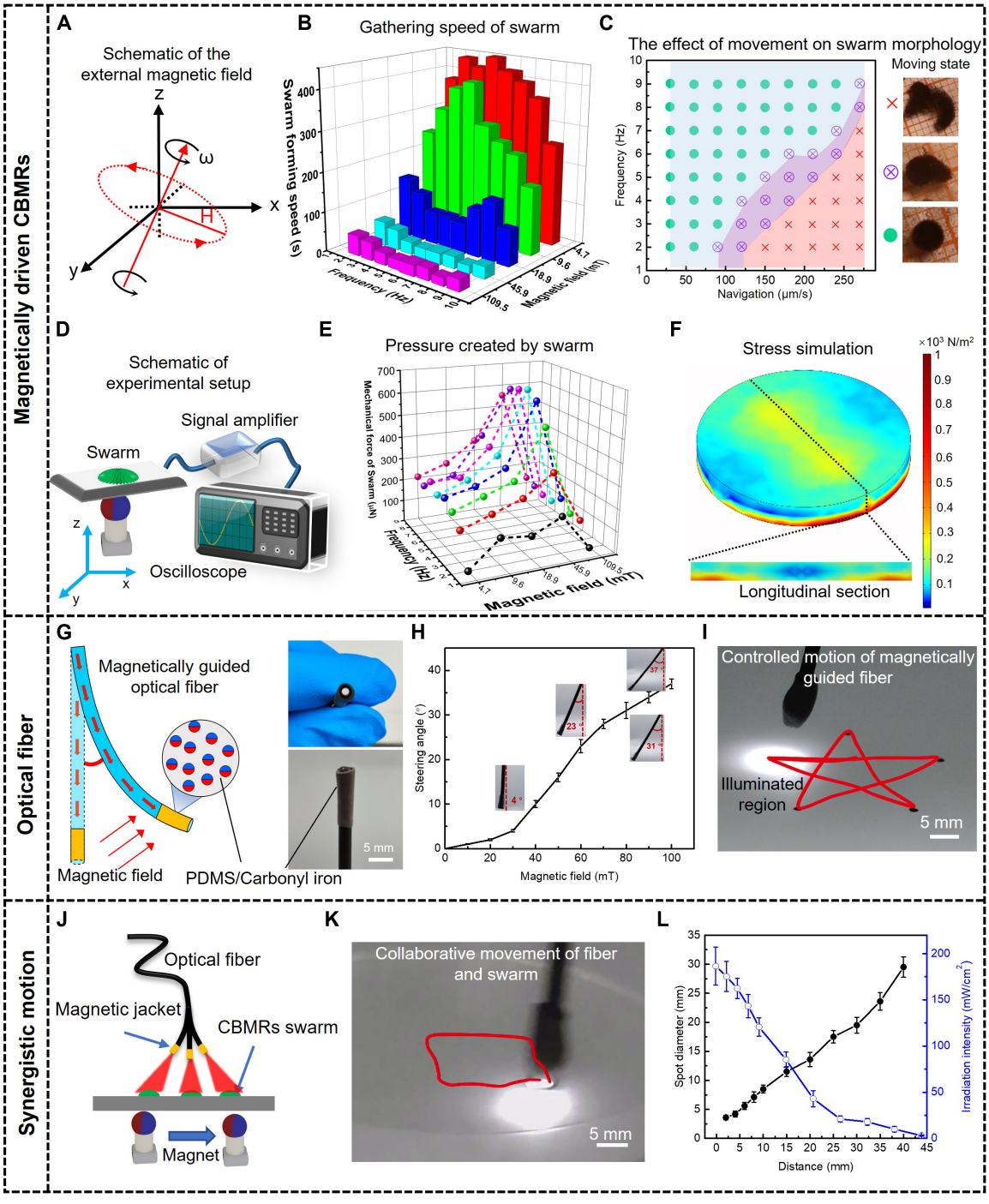

Fig. 3. Motion of a microrobot in a rotating magnetic field. (**A**) Schematic diagram illustrating the rotating magnetic field configuration. (**B**) The gathering speed of microrobot swarms under different strengths and frequencies of magnetic fields. (**C**) Effects of frequency and migration speed on the morphology and structural integrity of microrobot swarms (magnetic field intensity: 45.9 mT). Scale bars, 2 mm. (**D**) Schematic illustration of a device measuring microforces generated by microrobot swarms, using a piezoelectric film sensor. (**E**) Minute force (pressure) generated by swarming microrobots under various magnetic field conditions. (**F**) Simulated stress distribution generated by a microrobot swarm. (**G**) Schematic and optical images of a magnetically guided optical fiber. Scale bar, 5 mm. (**H**) Fiber bending angles under varying magnetic field intensities. Insets show representative bending images with scale bars of 5 mm. Data are presented as means ± SD (n = 3 independent experiments). (**I**) Programmed movement of the magnetically guided optical fiber under a static magnetic field. The red line represents the motion trajectory. Scale bar, 5 mm. (**J**) Schematic diagram depicting the coordinated movement of the magnetically guided optical fiber and microrobot swarm. (**K**) Recorded trajectory of the cooperative movement between the fiber tip and microrobot swarm. Scale bar, 5 mm. (**L**) Relationship between working distance, irradiation intensity, and spot size of the optical fiber. Data are presented as means ± SD (n = 3 independent experiments).

toward the bottom, thereby impeding their dynamic rotation. As simulated by a COMSOL Multiphysics model, the stress distribution is induced by the swarm (Fig. 3F). The swarm is simplified into a cylindrical shape. From the surface, it can be observed that the internal stress concentration primarily occurs at its poles, aligning with the distribution of magnetic flux density (fig. S12). Moreover, the axial profile of the swarm model reveals a noticeable gradient in stress distribution along its central axis, which can be attributed to the stronger magnetic flux densities close to the permanent magnet. This vertical stress enhancement induced by the magnetic field enables the swarm to generate sufficient pressure ranging from ~800 to 1000 μN, which is at the same order of magnitude as the measurements obtained using the piezoelectric film and indicates successful modeling.

Next, we developed a magnetically controllable optical fiber by coating a commercially available flexible optical fiber (diameter: 2 mm) with a magnetic jacket composed of carbonyl iron particles embedded in polydimethylsiloxane (PDMS), enabling precise magnetic manipulation (Fig. 3G). The driving force for the bending of the optical fiber comes from the interaction between the driving magnetic field and the magnetic particles dispersed in the polymer matrix (*34*). The presence of a magnetic sleeve induces the bending of the fiber under the influence of a magnetic field, as depicted in Fig. 3H. As the strength of the magnetic field increases, there is a gradual increase in the bending angle, reaching up to 37°. This offers a viable solution for achieving coordinated control over light source movement and microrobot swarms. Because of the exceptional bending capability of the optical fiber under the static magnetic field (Fig. 3I), the device efficiently completes the programmed motion according to the predesigned pentacle trajectory, demonstrating its ease of operation.

Given the swarming motion of microrobots under a high-frequency magnetic field, the motion stability of the optical fiber becomes crucial. If optical fibers can effectively track the swarming motion under such conditions, such tracking would enhance the application potential of CBMRs. The cooperative movement between the optical fiber and the microrobot swarm should be considered (Fig. 3J). It was seen that, in a dynamic magnetic field, the fiber exhibited unstable rotation (movie S2). Intriguingly, this rotation consistently revolved around the microrobot swarm under the irradiation of visible light from the optical fiber (Fig. 3K). On this basis, the variations of light spot size and light intensity with distances were studied (Fig. 3L). When at distances less than 10 mm, the magnetically guided optical fiber generated suitable spot sizes and light intensities to support ROS generation of CBMRs. At a working distance of ~5 mm, the fiber-generated spot effectively covered a large area while maintaining high irradiation intensity. Moreover, the effective irradiation region of the magnetic fiber increased with rising magnetic field strength. Specifically, at an intensity of 80 mT, the effective irradiation region of the magnetic fiber reached its peak value at 14.5 cm^2 (fig. S13). This result substantiates that our developed optomagnetic cooperative system could maintain swarming microrobots under continuous illumination of visible light without requiring further positioning, thereby facilitating continuous production of numerous free radicals for antibacterial purposes. The above characteristics are of paramount importance for subsequent antibacterial treatments. The development of a magnetically controlled optical fiber to follow the movement of swarming microrobots solves the challenge of activating the photochemical reaction of light-responsive microrobots in confined spaces, thus providing strong technical support for the successful treatment of inflammation in the deep cavity inside the human body.

In vitro biofilm eradication using CBMR swarms

Complete removal of the biofilm requires not only the destruction of its physical structure but also further chemical inactivation of the isolated bacteria to prevent biofilm regeneration. The antibacterial ability of CBMRs was first evaluated using *Escherichia coli* and *Staphylococcus aureus* via a plate counting method. BiOI and BMRs have little toxicity to bacteria under dark conditions (fig. S14). After 30 min of incubation, the survival rate of *E. coli* and *S. aureus* treated with CBMRs decreases to 70 and 60%, respectively, because of the bacteriostatic effect of Cu ions. As shown in Fig. 4A, the survival rate of *E. coli* and *S. aureus* treated with BiOI photocatalysts under visible-light irradiation decreased to 41.2% [1.1×10^7 colony-forming units (CFU)/ml] and 36.5% (2.1×10^7 CFU/ml), respectively. The survival rate of bacteria treated with BMRs in the rotating magnetic field was 32.4% (4.3×10^6 CFU/ml) and 15.8% (1.8×10^6 CFU/ml), respectively, which could be attributed to the movement of the microrobot in the rotating magnetic field that enhances the distribution of active free radicals. The bacterial survival rate after CBMR treatment decreased to less than 1% (<100 CFU/ml), indicating a strong synergistic antibacterial effect between Cu single atoms and BiOI photocatalytic activity. The antibacterial activity originates from the rational structural design of the CBMRs, resulting in the high-level production of ROS during light irradiation, which is a key step in the subsequent effective removal of biofilms.

To present the antibacterial results more intuitively, we analyzed all bacterial groups for live/dead activity by fluorescence microscopy imaging (Fig. 4B). Green fluorescence indicated that the bacteria remained viable, whereas red fluorescence intensity increased markedly after treatment with BiOI, BMRs, and especially CBMRs, suggesting substantial bacterial death, particularly in the CBMR-treated group. Moreover, the morphology of bacteria deformed and atrophied after treatment with BiOI, BMRs, and CBMRs (fig. S15). These results suggest that the bacteria dispersed in solution could be completely killed under the synergy of Cu single atoms and BiOI photocatalysis, demonstrating that CBMRs provided sufficient structural and chemical destruction to bacteria in suspension.

To ascertain the antibacterial mechanism of CBMRs, free radical scavengers [*p*-benzoquinone (p-BQ) to remove superoxide radicals, isopropyl alcohol (IPA) was used to remove hydroxyl radicals, potassium iodide was used to remove holes, and potassium dichromate, Cr(VI), was used to remove electrons] were introduced in the antibacterial experiment, and the results are shown in Fig. 4C. Compared with the control group, the bacterial survival rate increased after adding IPA. After adding p-BQ, the bacterial survival rate also increased, but the trend is not obvious. This indicates that the bacterial inactivation is caused by superoxide free radicals and hydroxyl free radicals, among which hydroxyl free radicals are the main active free radicals. To demonstrate the presence of hydroxyl radicals, we used terephthalic acid as a fluorescent probe to detect the hydroxyl radicals (fig. S16). The emission peak at 425 nm shows the fluorescence signal corresponding to hydroxyl radical (*35*). Electron paramagnetic resonance (EPR) spectroscopy was used to provide further verification of the hydroxyl radicals and superoxide radicals generated by BiOI, BMRs, and CBMRs upon exposure to visible-light irradiation. It is

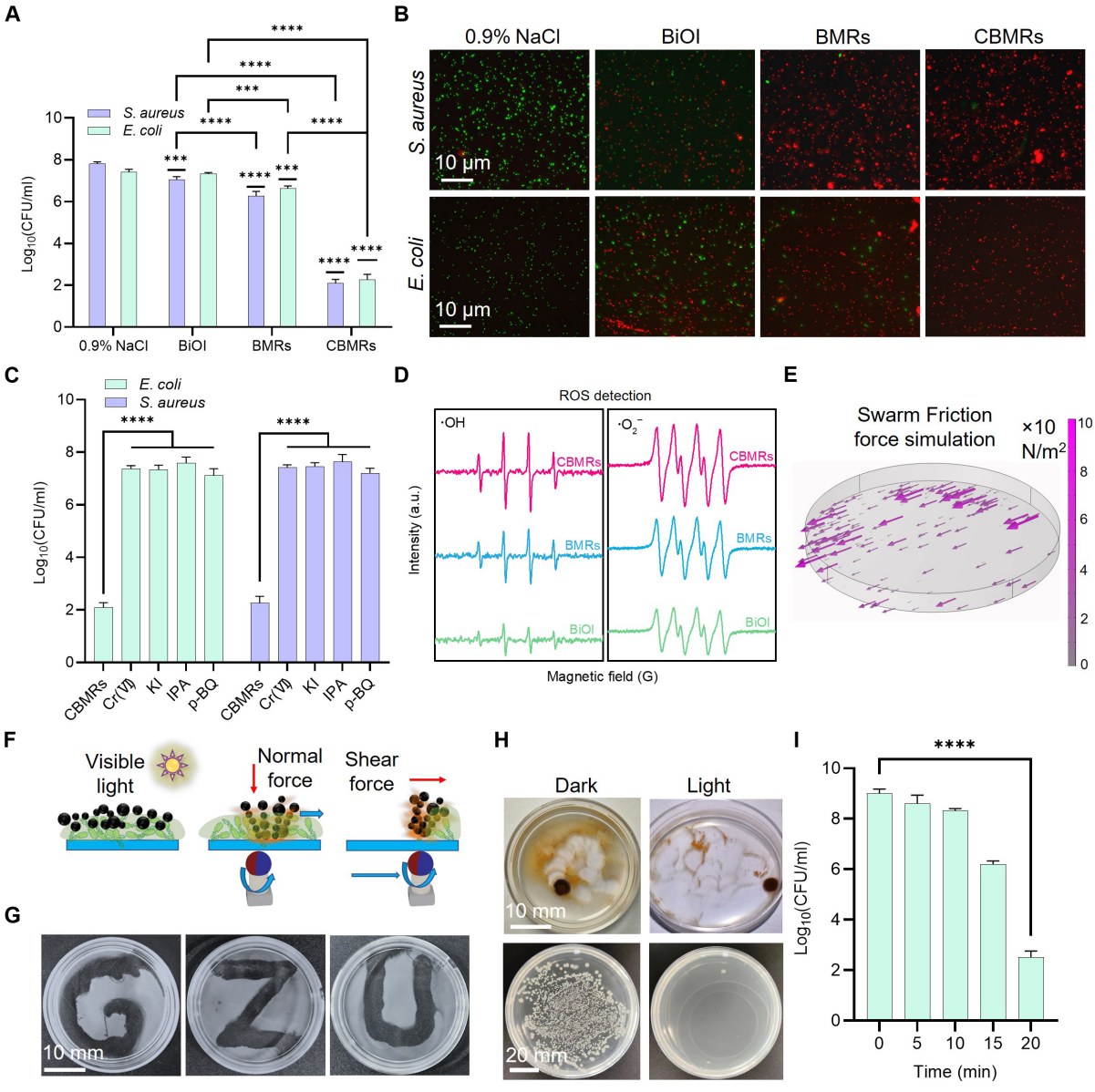

Fig. 4. Antibacterial properties and biofilm removal performance of CBMRs. (**A**) Antibacterial efficacy of CBMRs against *S. aureus* and *E. coli* under visible-light irradiation (200 mW/cm^2), a magnetic field of 10 mT, and a frequency of 7 Hz. Data represent means ± SD ($n = 3$ independent experiments; ***$P < 0.001$ and ****$P < 0.0001$). (**B**) Fluorescence microscopy images showing live/dead staining of bacteria after various treatments. Scale bars, 10 μm. (**C**) Influence of specific radical scavengers on antibacterial activity of CBMRs. Data represent means ± SD ($n = 3$ independent experiments; ****$P < 0.0001$). (**D**) EPR spectra detect hydroxyl radicals (•OH) and superoxide radicals (•O_2^-) produced by BiOI, BMRs, and CBMRs. (**E**) Simulation of frictional forces generated by the translational movement of the CBMR swarm under magnetic field actuation. (**F**) Schematic illustrating the mechanism of photocatalytic biofilm removal by CBMRs under magnetic field–induced axial and drag forces. (**G**) Photographs demonstrating precise removal of biofilms by magnetically actuated CBMRs. Scale bar, 10 mm. (**H**) Comparative images showing biofilm removal efficiency by CBMR swarms under dark and visible-light conditions. Scale bars, 10 mm (top) and 20 mm (bottom). (**I**) Time-dependent efficiency of biofilm eradication using a magnetically guided optical fiber combined with CBMR swarm. Data represent means ± SD ($n = 3$ independent experiments; ****$P < 0.0001$).

demonstrated in Fig. 4D that, after 10 min of illumination, CBMRs manifested notably strong signals associated with hydroxyl radicals and superoxide radicals (*36*), further indicating the synergistic effect of Cu single atoms and BiOI that results in the abundant generation of free radicals for antibacterial activity.

Photoelectrochemical tests showed that CBMRs have higher photocurrent density and lower interface charge transfer resistance than pristine BiOI nanosheets and Cu-free BiOI microrobots, thereby facilitating rapid ROS generation for bacterial inactivation (fig. S17). After reusing CBMRs seven times, the antibacterial rate against *E. coli* and *S. aureus* remained around 90%, demonstrating excellent stability (fig. S18). This indicates that numerous active free radicals produced through the synergistic effect of CBMRs and Cu atoms provide antibacterial activity, good stability, and higher antibacterial

efficiency compared with previously reported photocatalytic antibacterial microrobots (*37*). This antibacterial performance, combined with the magnetic actuation of the microrobots, achieves efficient destruction of biofilm through mechanical forces and chemical actions. The distribution of frictional force generated by swarm translation of CBMRs under a magnetic field was calculated using COMSOL software (Fig. 4E). Because of higher pressure at the poles, frictional forces increase in these regions. Under a rotating magnetic field, this results in elevated friction in the outer regions. Consequently, during biofilm removal processes, the peripheral region of the swarm exhibits the highest removal efficiency.

Figure 4F illustrates the mechanisms of biofilm removal by swarming CBMRs: photochemical activity and robust mechanical force. The polysaccharide shells that protect bacteria were destroyed by the axial forces of the swarming CBMRs. With the translation of the permanent magnet, large areas of biofilm were removed, allowing the bacteria to disperse in the solution (*38*). Under the irradiation of visible light, CBMRs produced abundant active free radicals to kill bacteria that were no longer protected by EPS.

As demonstrated in Fig. 4G, directional removal of biofilm was achieved by swarming CBMRs in a flat petri dish under a controlled path, indicating good controllability of the swarming CBMRs (movie S3), which is further supported by the fluorescence microscopy of biofilm staining (fig. S19). To consider the effect of illumination, we performed tests under dark and visible-light conditions (Fig. 4H). Under visible light, swarming CBMRs could remove all of the biofilm in the petri dish completely, but in the dark, only 50% of the biofilm was removed. This should be ascribed to the fact that the active free radicals produced by visible-light irradiation accelerate the decomposition rate of biofilm (*39*). Moreover, after incubation at 37°C for 18 hours, the bacterial solution treated under visible light was completely sterilized, whereas the bacteria treated in the dark remained dispersed and viable, posing a risk of biofilm regeneration. To validate the efficacy of CBMRs in eliminating biofilm when combined with the magnetically guided optical fiber, we cultured a microbiofilm in a 96-well plate, and CBMRs were induced with magnetic field actuation to form a swarm for assessing the cooperative removal of bacterial film. As depicted in Fig. 4I, the concentrated presence of CBMRs within a confined space enhanced their antibacterial effect, leading to complete eradication of the biofilm within 20 min. These results show that CBMRs can quickly and accurately remove biofilms under visible light, an effect attributable to both the mechanical destructive force brought about by the magnetic properties of CBMRs and the oxidation and bactericidal ability of the generated ROS. The simultaneous magnetic manipulation of the optical fiber and swarming motion of CBMRs for collaborative antibacterial action offers a solution for eradicating inflammation caused by deep biofilm infections inside the human body.

Ex vivo assessment in a porcine sinusitis model

Next, it was explored whether CBMRs effectively remove biofilms from the surface of biological tissues. *S. aureus* is one of many bacteria that cause sinusitis infections (*40*, *41*), so it was used to grow biofilms in the sinuses of pigs. The ability of swarming CBMRs, with the assistance of an optical fiber, to remove biofilm in pig sinuses was evaluated in vitro. The experimental process is illustrated in Fig. 5A. Specifically, CBMRs (0.5 ml) were injected into the pig sinuses, and a 2-mm-diameter optical fiber was extended from the xenon lamp and inserted through the nasal cavity into the sinuses. Swarming CBMRs were externally controlled with a permanent magnet. As observed, numerous yellow biofilms were present on the surface of the sinuses before treatment, and they disappeared after CBMR treatment (Fig. 5B). The treated bacterial solution after live/dead fluorescent probe staining is shown and compared in Fig. 5C. A substantial amount of green fluorescence indicated viable, untreated bacteria, and visible-light irradiation alone had little effect on the fluorescence activity of bacteria. When treated with CBMRs under visible light, a sharp increase occurred in red fluorescence intensity, indicating a high amount of bacterial death. The above results demonstrate that CBMRs could remove biofilms in pig sinuses because of the synergistic effect of Cu single atoms and photocatalysis.

The MTT cell viability assay [3-(4,5-dimethylthiazol-2-yl)-2,5-diphenyltetrazolium bromide assay] in Fig. 5D shows that the survival rates of bacteria treated with visible light alone, CBMRs under dark conditions, and CBMRs under visible light are 93, 70, and 3%, respectively, which is further supported by the results of plate culture (fig. S20). Therefore, these results verify that CBMRs could easily remove biofilm from the surface of animal tissue, providing favorable evidence for the application of CBMRs in a living sinusitis model. To further assess the in vivo application, we examined the effects of irradiation intensity and dosage on the antibacterial activity of CBMRs (fig. S21). When the concentration of CBMRs for injections reached 250 μg/ml and the optical density reached 150 mW/cm^2, effective eradication of porcine sinus biofilm could be achieved. Meanwhile, the biocompatibility of CBMRs was investigated. As shown in Fig. 5E, mouse stem cells were cultured together with CBMRs. After irradiation, the cell survival rate remained above 90%, suggesting good safety. The toxicity tests for different dosages of CBMRs further indicate that CBMRs had good biocompatibility for subsequent experiments (fig. S22), supported by the live/dead fluorescence staining (Fig. 5F). The ion release profile further demonstrates that the stability of CBMRs can effectively mitigate the adverse effects associated with the release of metal ions (fig. S23). In summary, in vitro experiments demonstrate that CBMRs have good mechanical properties and the ability to remove sinus biofilm. When combined with the magnetically guided optical fiber to introduce visible light into the sinuses, the established platform is expected to be effective for the treatment of real biological sinusitis.

CBMR propulsion through sinusitis-associated biological barriers in vitro and in vivo

The immune response triggered by biofilm infection leads to the local production of a substantial number of inflammatory secretions, which form a biological barrier that presents a major challenge to the precise targeting of microrobots (*42*, *43*). Therefore, microrobots need not only to be efficient in sterilization but also to have a strong ability to penetrate biological barriers for practical application scenarios (*44*). To establish a sinusitis model conveniently and cost-effectively, we used rabbits as experimental subjects (*45*, *46*). A suspension of *S. aureus* liquid was injected into the maxillary sinuses of rabbits, causing a bacterial infection and then a severe inflammatory response in the sinus mucosa. After 5 days of feeding, a large amount of white inflammatory secretion formed in the rabbit sinusitis (fig. S24). As shown in Fig. 6A, CBMRs must cross a biological barrier formed by inflammatory secretion to reach the mucosal surface of the sinuses and remove the biofilm. Therefore, further research on the composition and properties of biological barriers

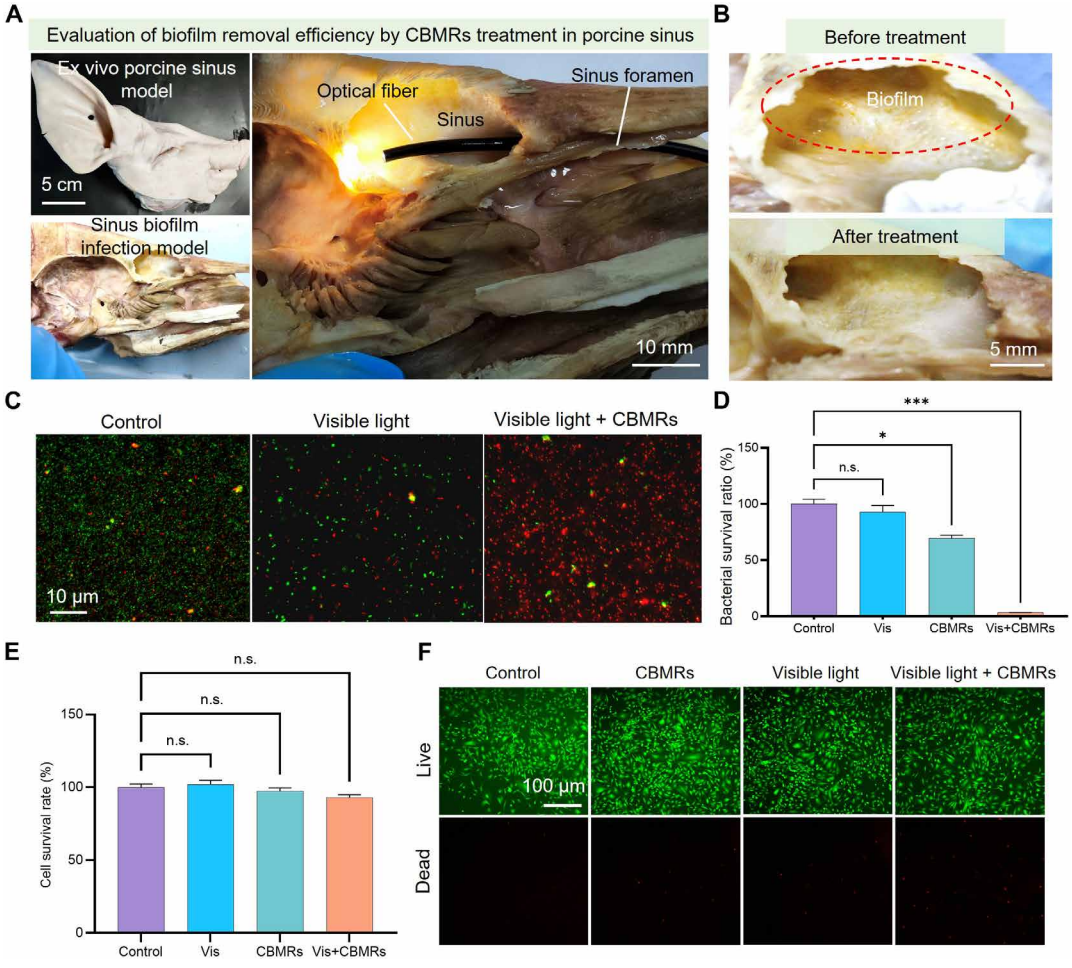

Fig. 5. Ex vivo validation of photomagnetic synergistic antibacterial therapy using CBMRs. (**A**) Experimental procedure of biofilm formation and subsequent CBMR-assisted photomagnetic therapy in a porcine sinusitis model. Scale bars, 5 and 10 mm. (**B**) Representative macroscopic images of porcine sinuses demonstrating biofilm presence before and after photomagnetic synergistic treatment. Scale bar, 5 mm. (**C**) Live/dead fluorescence staining of bacteria extracted from biofilms treated under various conditions: untreated (control), visible-light irradiation alone (Vis), and visible light combined with CBMRs (Vis + CBMRs). Green indicates viable bacteria; red indicates dead bacteria. Scale bar, 10 μm. (**D**) Quantitative bacterial viability analysis using MTT assay after different treatments. Data are presented as means ± SD ($n = 3$ independent biological samples; $^{*}P < 0.05$ and $^{***}P < 0.001$). (**E**) Cytotoxicity assessment of CBMRs on mouse stem cells measured by CCK-8 assay. Data represent means ± SD ($n = 5$ independent samples; n.s., not significant). (**F**) Representative live/dead fluorescence staining images of mouse stem cells treated with CBMRs under visible light. Scale bar, 100 μm. Cells stained green indicate viability, and red indicates dead cells.

is needed. The inflammatory secretion filled the entire sinuses, suggesting the formation of a biological barrier in the sinuses (Fig. 6B). This biological barrier encompasses deceased immune cells, goblet cells, and bacterial secretions, and it is different from normal mucus, which primarily consists of inorganic salts, water, and mucus. Experiments simulating the penetration of CBMR swarms through inflammatory secretions were performed in a tubular model. Under the magnetic field, although some microrobots were blocked, the swarm quickly passed through the barrier (Fig. 6C).

This observation demonstrates that CBMR swarms exhibit enhanced penetration capability toward inflammatory secretions when subjected to an external magnetic field. However, penetration efficiency relying solely on mechanically driven magnetic forces remains limited. To assess the contribution of the light field to biological barrier penetration, we examined the motion of CBMRs in various biological fluids under magnetic fields (Fig. 6D). Under dark conditions, CBMRs exhibited the highest velocity in urine (20 μm/s), whereas slightly reduced velocities were observed in lung fluid and sinus mucus because of their higher viscosity. However, in the highly viscous intestinal fluid and inflammatory secretion, the velocities of CBMRs decreased to 8.2 and 4.3 μm/s, respectively, because of greater viscous resistance. Upon exposure to visible light, the velocities of CBMRs increased across all samples, particularly in intestinal fluid and inflammatory secretions, reaching 14.5 and 10.2 μm/s, respectively. Thermal effects have previously been shown to facilitate microrobot penetration through biological barriers (*16*). The observed increase in CBMR mobility can be attributed to localized temperature elevation induced by visible-light irradiation, reducing mucus viscosity and consequently diminishing viscous resistance encountered by CBMRs. The temperature elevation of CBMRs under visible-light irradiation was monitored using infrared thermography, as depicted in Fig. 6E. Upon illumination, CBMRs rapidly increase in temperature, reaching ~55.6°C within 5 min. This photothermal effect originates from the exceptional light absorption of CBMR swarms, which facilitates

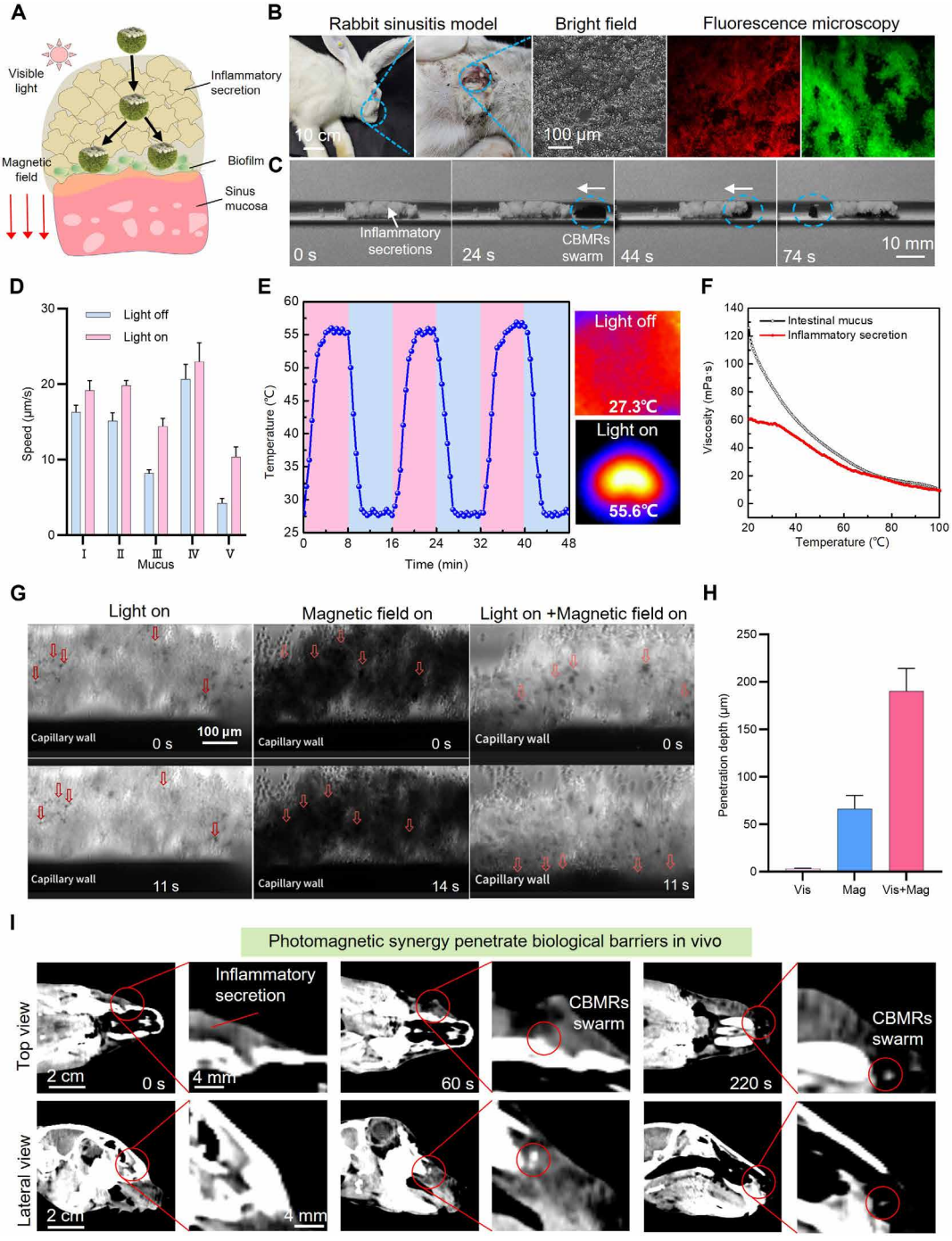

Fig. 6. Photomagnetic synergy enhances CBMR penetration through biological barriers in vitro and in vivo. (**A**) Illustration showing CBMR swarm penetrating biofilm and inflammatory secretions to reach the underlying sinus mucosa. (**B**) Establishment and characterization of the rabbit sinusitis model. Optical images depict infected rabbit sinuses, with bright-field microscopy and fluorescence imaging (red and green channels indicating dead and live cells, respectively) demonstrating inflammatory secretion composition. Scale bars, 10 cm (rabbit) and 100 μm (microscopy images). (**C**) Time-lapse images illustrating CBMR swarm penetration through inflammatory secretion under magnetic field actuation. Scale bar, 10 mm. (**D**) Quantitative analysis of CBMR velocity enhancement by photothermal effect in mucus samples: pulmonary fluid (I), sinus mucus (II), intestinal mucus (III), urine (IV), and inflammatory secretion (V). Experimental conditions: magnetic field intensity, 10 mT; frequency, 7 Hz. Data represent means ± SD ($n = 3$). (**E**) Temperature profile showing repeated photothermal heating cycles of the CBMR swarm under visible-light irradiation, with corresponding infrared thermography images displaying temperature distribution. (**F**) Temperature-dependent viscosity reduction of intestinal mucus and sinus inflammatory secretion, illustrating fluidization upon heating. (**G**) Time-lapse microscopy images demonstrating CBMR particle penetration into biological barriers under three different actuation modes. Scale bar, 100 μm. (**H**) Quantitative comparison of CBMR penetration depths achieved under the three actuation conditions. Data represent means ± SD ($n = 3$). (**I**) Real-time CT imaging illustrating in vivo CBMR swarm penetration through biological barriers within rabbit sinuses, enhanced by combined photomagnetic synergy at different time points (0, 60, and 220 s). Scale bars, 2 cm (top and bottom left) and 4 mm (enlarged regions).

efficient heat accumulation. To investigate temperature-induced changes in liquid properties, we examined rheological characteristics for high-viscosity intestinal fluid and inflammatory secretions at various temperatures (Fig. 6F). The viscosity of both intestinal fluid and inflammatory secretions decreased upon heating. The viscosity of inflammatory secretions at 50°C decreased to less than one-third of its value at 20°C. Such viscosity reduction enhances fluid mobility, lowering the viscous resistance encountered by CBMRs and thereby increasing their penetration speed. These findings highlight the capability of the collaborative photomagnetic therapeutic platform to simultaneously enhance biological barrier permeability and antibacterial efficacy.

Moreover, temperature elevation enhances the catalytic reaction rate and augments the efficiency of ROS generation, thereby further bolstering the antibacterial efficacy of the photothermal process (*47*, *48*). As depicted in fig. S25A, an increase in the fluorescence signal of hydroxyl radicals was observed after the temperature rise. When the dosage of CBMRs remained constant, higher temperatures led to enhanced antibacterial efficacy. Capillary tubes were used to simulate the sinus cavity, and CBMRs were precisely guided through inflammatory secretions by external magnetic fields (fig. S25B).

As shown in Fig. 6G, the microrobot motion was tested under illuminated and dark conditions. Under the dark condition, the single CBMRs moved slowly under the magnetic field because of resistance from the biological barrier, thus failing to reach the capillary wall quickly (movie S4). After the light was activated, the biological barrier exhibited increased fluidity, which can be ascribed to the temperature of inflammatory secretions accelerating their internal motion. The application of the magnetic field enabled the CBMRs to easily penetrate the biological barrier and reach the capillary wall. Figure 6H shows the displacement of CBMRs in the three modes over identical time intervals. When the particles were exposed to light alone, they showed Brownian motion, and the moving region remained nearly unchanged. When the CBMRs were controlled by a magnetic field alone, they moved toward the capillary wall, achieving a displacement of 65 μm. However, when the light and magnetic field worked together, the displacement increased to 191 μm. This comparative analysis further substantiates the efficacy of combining optical and magnetic fields to augment the penetrative capacity of CBMRs across biological barriers, thereby enabling rapid deployment to sites of inflammation and infection.

To verify the clinical applicability of enhanced penetration through biological barriers, we conducted in vivo experiments in the sinuses of rabbits with sinusitis. The process of CBMRs penetrating the biological barrier in rabbit sinuses was recorded using computed tomography (CT) technology, as illustrated in Fig. 6I. The CT image shows the low-contrast-density biological barrier formed by purulent secretions in the maxillary sinus. At 60 s after injection and magnetic actuation, a distinct CBMR swarm was visualized within the sinus. Under the combined influence of optical fibers and the magnetic field, the swarm formed by CBMRs successfully crossed the biological barrier and reached the bottom of the maxillary sinus after 220 s. These results demonstrate clinical potential for the photomagnetic synergistic strategy to enhance microrobot penetration through biological barriers. The ability of CBMRs to penetrate biological barriers and remove biofilms was further verified (fig. S26). Under irradiation of visible light, a swarm formed by CBMRs successfully penetrated the biological barrier formed by inflammatory secretions to reach the biofilm surface and directionally disrupt the biofilm under mechanical forces exerted by the swarm (movie S5). Both single particles and a swarm of CBMRs rapidly penetrated the biological barrier formed by sinusitis under the synergistic effect of light and magnetic field and aggregated on the surface of the sinus mucosa to effectively remove biofilms. The successful implementation of CBMRs in the sinusitis model to enhance their penetration into biological barriers under the synergy of light and magnetic fields provides theoretical support for the treatment of sinusitis in vivo.

In vivo photocatalytic therapy in rabbit sinusitis using CBMRs

The photomagnetic synergistic therapy based on the developed CBMRs exhibits notable advantages in terms of potent antibacterial activity and enhanced penetration through biological barriers. However, certain challenges remain that need to be addressed for its effective implementation in vivo. In terms of complex clinical conditions, the precise positioning and navigation capabilities of microrobots play a pivotal role (*49*, *50*). Thus, the New Zealand rabbit sinusitis infection model was used to evaluate the therapeutic effect of a combined optomagnetic platform consisting of a magnetically guided optical fiber and CBMRs. A photocatalytic processing system, mainly consisting of DR imaging, a xenon lamp light source system, an optical fiber, and a magnetic actuation system, was used to assist the treatment of rabbit sinusitis with CBMRs (Fig. 7A). Because of its rapidity, convenience, and cost-effectiveness, DR imaging was chosen for real-time tracking of CBMR movement. We also examined the influences of magnetic field intensity and CBMR dosage on DR imaging quality (fig. S27). The results indicate that a distinct imaging contrast was achieved in rabbit sinuses when the magnetic field intensity exceeded 45.9 mT and the CBMR dose surpassed 300 μl.

The infected sinus side of the rabbits was treated, and the entire treatment process was divided into three stages (Fig. 7B). In stage 1, CBMRs were injected into the sinus entrance through a catheter and migrated under magnetic actuation toward the biological barrier formed by inflammatory secretions. In stage 2, the temperature of the CBMRs swarm increased because of the photothermal effect generated under the visible-light irradiation. The viscosity of the biological barrier decreased, and the fluidity increased with the increase in temperature. Upon applying the external magnetic field, CBMRs quickly passed through the biological barrier and reached the site of bacterial infection. In stage 3, the CBMRs swarm began to destroy the biofilm. CBMRs produced many ROS for antibacterial activity under the coordination of photocatalytic BiOI and Cu single atoms. Eventually, the synergy of magnetically induced force and photocatalytic effects eradicated the biofilm, thereby alleviating the inflammatory response. In addition, the movement of the skull part was achieved through a three-position magnet motion. The visible light used was filtered through a 420-nm cutoff filter. It was demonstrated in the cell coculture experiment that exposure to visible light for 20 min did not induce detectable cytotoxicity. In the subsequent animal experiment, each area received a treatment time of 15 min, ensuring no adverse effects on the rabbit's nasal mucosa. The rotational movement of only a portion of the optical fiber magnetic head during treatment minimized its influence on the sinuses, thereby ensuring complete preservation of the sinus mucosa without any damage. This treatment protocol combines the navigational motion characteristics of the robot with the ability to effectively remove biofilms, allowing for the noninvasive treatment of inflammation in small and complex spaces.

Given the location of the sinuses within the skull and their proximity to high-density regions, capturing clear images of CBMR motion

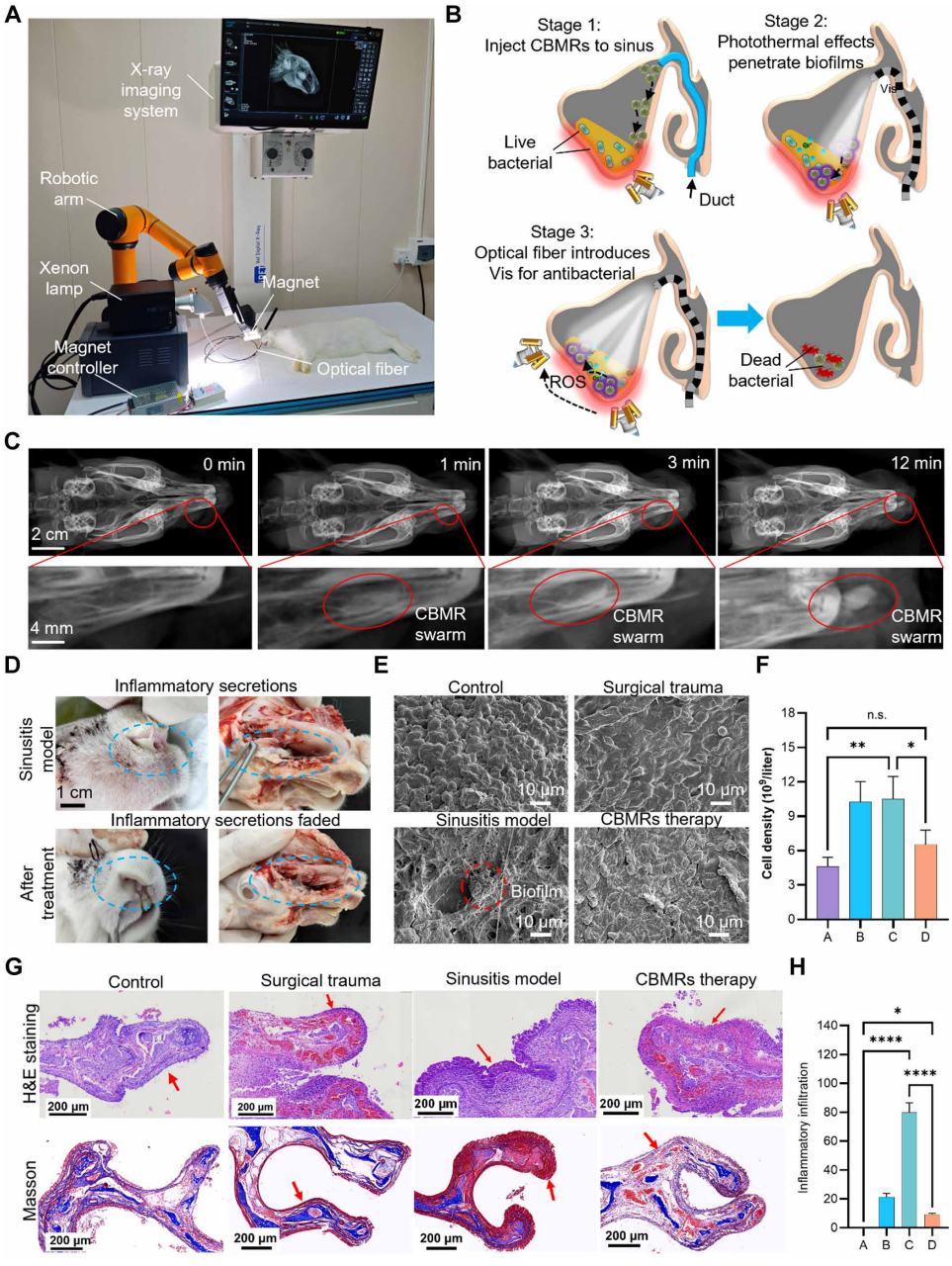

Fig. 7. Photomagnetic synergistic therapy of sinusitis using CBMRs in a rabbit model. (**A**) Experimental setup showing the integrated photomagnetic therapeutic platform, composed of a robotic magnetic control system, a xenon lamp illumination source coupled to an optical fiber, and an x-ray imaging device for real-time monitoring. (**B**) Schematic illustration depicting the delivery, penetration, and antibacterial treatment of CBMRs within sinus cavities through photomagnetic synergistic actions. (**C**) Time-lapse x-ray images demonstrating precise magnetic navigation and accumulation of CBMR swarm inside the rabbit sinus. Scale bars, 2 cm (DR images) and 4 mm (enlarged regions). (**D**) Optical images comparing the external nasal regions and internal sinus anatomy of the rabbits before and after CBMR therapy, indicating clearance of inflammatory secretions. Scale bar, 1 cm. (**E**) SEM images comparing sinus mucosal surfaces among different groups (top: untreated sinusitis model showing prominent biofilm structures; bottom: CBMR-treated sinus with minimal biofilm presence). Scale bars, 10 μm. (**F**) Quantitative evaluation of white blood cell infiltration levels in rabbit sinus tissues among various experimental groups (A, healthy control; B, surgical trauma control; C, untreated sinusitis model; and D, CBMR-treated group). (**G**) Histological images of sinus mucosa tissues collected 3 days posttreatment, stained by H&E (top) and Masson's trichrome (bottom). Red arrows indicate regions of inflammatory cell infiltration. Scale bars, 200 μm. (**H**) Quantitative measurement of inflammatory infiltration thickness in sinus mucosal tissues from each experimental group, confirming therapeutic effects after CBMR treatment. Data in (F) and (H) are presented as means ± SD ($n = 3$ independent biological replicates). Statistical significance is indicated as $^{*}P < 0.05$, $^{**}P < 0.01$, and $^{****}P < 0.0001$.

poses a substantial challenge (*51*). Therefore, we first investigated intrasinus x-ray imaging of CBMRs. The forward x-ray imaging of CBMRs in the rabbit sinus initially showed that CBMRs were dispersed with low imaging contrast and could not be observed (Fig. 7C). However, after applying a magnetic field for 1 min, a swarm formed at the sinus opening, leading to an improvement in imaging contrast because of increased density within the region. During the movement of the magnetic field, a swarm of CBMRs could be observed, demonstrating strong controllability in in vivo experiments. Furthermore, coordinated photomagnetic movement for 12 min successfully guided the swarm from the entrance to reach the bottom of the sinuses, as confirmed by lateral x-ray imaging (fig. S27D). CBMRs exhibited distinct imaging contrast under x-ray and could be efficiently deployed in infected areas within the sinuses through cooperative manipulation of both magnetic and light fields.

The rabbit model of sinusitis was treated using the aforementioned procedure, and the therapeutic effect was evaluated by appearance, routine blood detection, and tissue staining. Optical images of the rabbit nasal region before and after photocatalytic treatments with magnetically driven CBMRs (Fig. 7D) show distinct differences. Before treatment, the rabbits exhibited runny noses and obstructed breathing on the inflamed sinus side. After treatment, nasal discharge disappeared, and respiratory rates returned to normal. Rabbits were euthanized, and their sinuses were dissected. Internal optical photographs revealed abundant white inflammatory secretions in the sinuses before treatment, which were reduced after therapy. Simultaneously, microscopic observation of sinus mucus after treatment (fig. S28) indicated a notable reduction in cell counts. In addition, live/dead fluorescence staining demonstrated no detectable green fluorescence signals, indicative of live cells or bacteria, suggesting diminished cell shedding and a reduced immune response in the sinus mucosa after treatment.

Biofilm infections often cause severe damage to the sinus mucosa. To further investigate mucosal recovery after photomagnetic therapy, we used electron microscopy to analyze sinus mucosal surfaces from rabbits in each intervention group

(Fig. 7E). Epithelial cells on the sinus mucosal surfaces in the control and surgical trauma groups exhibit well-organized and densely packed structures. Conversely, the sinusitis model displayed extensive epithelial cell shedding and deformation, accompanied by evident *S. aureus* biofilm formation on the mucosal surface (*45*). After treatment with CBMRs under photomagnetic actuation, epithelial cells on the sinus mucosa, although not fully realigned, showed largely restored morphology, indicating that this treatment effectively eradicated biofilm infections and promoted mucosal repair. These optical and SEM analyses provide preliminary evidence for successful sinusitis treatment in rabbits.

Routine blood tests were conducted in the control, model, surgical trauma, and treatment groups. The red blood cell count data (fig. S29) were comparable to those of the control group. As shown in Fig. 7F, the white blood cell count in the sinusitis model group was elevated, confirming active inflammation. White blood cells decreased in the treatment group, indicating alleviation of inflammation. Further classification of white blood cells revealed additional details in fig. S30. Lymphocytes in the sinusitis model group were nearly absent, signifying severe bacterial inflammation in rabbits, whereas lymphocyte counts gradually returned to normal after CBMR treatment (fig. S30A). Monocytes and neutrophils showed similar trends (fig. S30, B and C). Posttreatment CBMR administration led to a substantial reduction in white blood cells, further validating the alleviation of inflammation. These hematological results confirm the effectiveness of the CBMR-mediated catalytic therapeutic system for rabbit sinusitis treatment.

To directly verify therapeutic efficacy in rabbit sinusitis, we performed Masson's trichrome and hematoxylin and eosin (H&E) staining on sinus mucosal tissues after euthanasia to evaluate epithelial structure and collagen fiber formation. In Fig. 7G, H&E staining of the sinusitis model revealed extensive inflammatory infiltration (marked by blue staining). After treatment, mucosal staining became predominantly red, indicating reduced inflammatory cell infiltration. Masson's trichrome staining assessed collagen fiber formation, where inflammatory conditions typically result in severe fibrosis (red staining areas) (*52*). Figure 7H quantifies the thickness of collagen fiber layers. The sinusitis model exhibited severe fibrosis, with collagen fiber thickness measuring ~78.6 μm. After CBMR treatment, collagen fiber thickness was reduced to ~10.3 μm, indicating successful sinusitis treatment and gradual restoration of sinus mucosal function after biofilm eradication. After ciliary cell function recovery, residual CBMRs within the sinuses could be excreted with nasal mucus through ciliary action. Last, the potential physiological toxicity of CBMRs to major rabbit organs was assessed by H&E staining (fig. S31). No obvious tissue damage was observed in the experimental group, confirming the biocompatibility of CBMRs in vivo.

Comprehensive evaluations, including nasal anatomy, hematological parameters, and histological analyses, demonstrate that CBMRs combined with magnetically guided optical fiber–mediated photocatalysis represent a highly effective therapeutic platform for sinusitis treatment. Overall, we have developed a multifunctional in vivo antimicrobial therapeutic platform using CBMR microrobots. This platform synergistically combines precise microrobot navigation, photocatalytic antibacterial properties, and Cu single atom catalysis, achieving targeted biofilm eradication within biological tissues under magnetically driven optical fiber guidance.

DISCUSSION

Magnetically driven micro- and nanorobots play a pivotal role in active targeted therapy for precision medicine. However, the clinical translation of magnetically driven micro- and nanorobots for biofilm eradication faces two critical challenges: Highly viscous inflammatory secretions form physical barriers that impede effective robot penetration, and currently available therapeutic agents lack sufficient antibacterial efficacy against established biofilms. In this work, we developed a photomagnetic synergistic therapeutic platform using photocatalytic microrobots (CBMRs) comprising single-atom copper-loaded BiOI catalysts and SiO_2-coated Fe_3O_4 magnetic particles. This integrated approach leverages both photothermal effects and magnetic actuation to enhance microrobot penetration through biological barriers and facilitate precise localization at deep infection sites. The CBMRs rapidly generate ROS under visible-light irradiation, providing robust antibacterial activity and overcoming resistance posed by viscous inflammatory secretions, thereby substantially enhancing therapeutic efficacy in targeted biofilm eradication.

Through experimental investigations, we have elucidated the motion characteristics, control parameters, and mechanical properties of swarming CBMRs. These microrobots demonstrate antimicrobial activity under visible-light irradiation and can effectively eliminate bacteria within confined anatomical spaces. The combined mechanical force generated by magnetic fields and the photothermal effect induced by visible light enables efficient penetration through biological barriers, facilitating rapid biofilm removal via chemical reactions. Moreover, CBMRs exhibit excellent stability and can be reused multiple times. In addition, we have developed a magnetically guided optical fiber to achieve integrated control of the magnetic field, optical fiber, and swarm behavior. By manipulating the magnetic field, we guided the optical fiber to track the swarm's movement and maintain its continuous activation, thereby maximizing efficiency in dynamic biofilm removal. Our sinusitis treatment platform based on CBMRs demonstrated successful in vivo implementation of photocatalytic antibacterial therapy using an optical fiber in rabbit models.

In summary, our proposed microrobotic therapeutic platform offers the advantages of noninvasiveness, minimal resistance, and drug-free intervention. This single-atom photocatalyst-based treatment approach not only reduces overall costs but also provides a versatile solution for treating other sinus-related diseases. Moreover, it will mitigate the risks associated with clinical surgery, holding promising implications for real-world clinical applications.

MATERIALS AND METHODS

Materials

Ferric chloride hexahydrate, ethylene glycol, sodium acetate, polyethylene glycol (molecular weight = 10,000), potassium iodide, bismuth nitrate pentahydrate, copper chloride, sodium borohydride, tetraethyl silicate, and 3-aminopropyltriethoxysilane (APTES) were purchased from Aladdin Reagent Company (USA). All chemicals were analytical and could be used without further purification. Deionized water was used in all experiments.

Fabrication of BMRs

Fe_3O_4 was prepared according to the reported method. Fe_3O_4 nanoparticles were weighed and dispersed in deionized water (1 mg/ml), and then anhydrous ethanol (4 ml) and ammonia (250 μl) were added. After ultrasonic stirring, 20 μl of ethyl tetrasilicate was

quickly added. After ultrasonic reaction for 4 hours, APTES (200 μl) was added to continue the ultrasonic reaction for 4 hours. The precipitation was collected by centrifugation and cleaned several times, and the magnetic nanoparticles were obtained after drying Fe_3O_4@SiO_2 (53). Fe_3O_4@SiO_2 was dispersed in aqueous solution, sprayed evenly on the surface of the slide, and dried for later use. Bismuth nitrate pentahydrate (0.6 g) was weighed, dissolved in 60 ml of a methanol and ethylene glycol (1:1) mixture, completely dissolved in 0.2053 g of potassium iodide, and ultrasonically reacted for 30 min. The slide was inserted diagonally into the Teflon lining so that the reaction precursor was completely immersed in the slide and reacted at 160°C for 12 hours. The growth layer of the slide was removed by ultrasound, and the product was collected by magnet, washed with deionized water and ethanol, and then dried to obtain BMRs.

Fabrication of CBMRs

BMRs (50 mg) were dispersed in 2 mM copper chloride solution (2 ml) for ultrasound for 30 min, and then 200 μl of sodium borohydride solution (0.1 M) was added for ultrasound for 30 min. The precipitation was collected by centrifugation, washed three times in deionized water, and then freeze-dried to obtain CBMRs.

Design of magnetically guided optical fiber

The carbonyl iron powder was mixed with PDMS at a mass ratio of 1:1, the optical fiber was inserted into the mixing slurry, the magnetic shell was uniformly coated, and last, the magnetic shell was cured by an infrared lamp for 2 min.

Magnetic actuation of CBMRs

The magnetic actuation experiments for both individual and swarms of CBMRs were conducted as follows: For individual CBMR actuation, the CBMRs were dispersed in water and observed using a Tesla coil setup combined with a microscope equipped with a 40× objective lens. A custom-built controlled magnetic field was applied transversely to induce rotation. For swarm actuation, CBMRs were dispersed in water at a concentration of 5 mg/ml, and a 3D-printed stepper motor platform controlled the rotation of a permanent magnet to generate swarm motion. The magnetic field's rotation frequency was determined by dividing the rotation speed by 60.

Evaluation of antibacterial activity

E. coli cultured in BHI (brain heart infusion) and *S. aureus* cultured in Luria-Bertani (LB) medium were used for antibacterial experiments. Bacteria were diluted with normal saline to 10^7 CFU/ml. Material was added to 3 ml of bacterial solution, and the solution was stirred in the dark for 30 min, irradiated under visible light for 30 min, and used for the antibacterial experiment. The antibacterial activity of BMRs and CBMRs was evaluated in the magnetic field generated by the Tesla coil with a magnetic field intensity of 10 mT and a frequency of 7 Hz. In addition, the bacteriostatic ability of each sample was evaluated by the plate count method. The specific method was to smear 10 μl of bacterial solution on an agar plate and culture the plate in a constant temperature incubator at 37°C for 16 hours. Statistical analysis was performed by Image software.

Biofilm culture

Glucose (1.5%) was added to the BHI medium, *S. aureus* was diluted to 10^8 CFU/ml using the modified medium, and 3 ml of bacterial solution was added to the 35-mm petri dish. The biofilm was obtained by culturing at 37°C for 8 hours.

Optic fiber combination with CBMRs for biofilm removal

According to the aforementioned method, the biofilm was cultured in a 96-well plate. After aspirating the medium, 500 μl of phosphate-buffered saline (PBS) buffer solution was added, followed by the addition of CBMRs (200 μg/ml). A swarm formed under a rotating permanent magnet for biofilm removal as visible light from xenon lamps was delivered into the 96-well plate via optical fibers. The light intensity was regulated by adjusting the current of the xenon lamp. After the reaction, the bacterial solution was diluted, and plate counting was performed to evaluate the antibacterial activity.

In vitro experimental validation of biofilm removal from porcine nasal sinuses

Freshly slaughtered pig heads were obtained from an abattoir, where the animals had been previously slaughtered for consumption. Because the tissue was collected post-mortem from animals processed for food, the study was exempt from institutional animal care. Three milliliters of an *S. aureus* suspension (1.5 % w/v glucose) was injected into each sinus cavity, and the sinuses were cultured at 27°C for 12 hours to grow biofilms. Second, the optical fiber connected to the xenon lamp was inserted through the nasal cavity of the pig into the sinus, 0.5 ml of CBMR solution (200 μg/ml) was injected, and then the biofilm was removed through the optical fiber and the permanent magnet. After treatment, the remaining bacterial solution was collected for live/dead staining and MTT detection.

Cytotoxicity testing of CBMRs

Mouse stem cells were cultured in 96-well plates with 5000 cells. CBMRs with concentrations of 10, 25, 50, 100, 150, and 250 μg/ml were added, respectively, and five samples were prepared in parallel for each concentration group. The pore plates were irradiated under visible light for 15 min, cultured in a constant temperature incubator at 37°C for 24 hours, and injected with 10 μl of a Cell Counting Kit-8 (CCK-8) solution, and an absorbance test was carried out 4 hours after the reaction started. The average value was compared with the blank group to calculate the cell survival rate.

Viscosity of mucus

The viscosity changes of different slimes were detected by rheometer during the heating process, and the heating rate was 5°C/min. To avoid evaporation loss during the heating process, we performed oil sealing before the test.

Rabbit model of sinusitis

Twenty-four healthy male New Zealand rabbits (age: 8 to 12 weeks; weight: 1.8 to 2.5 kg) were obtained from Shenzhen Lingfu Top Biotechnology Co. Ltd. Animals were housed under standard laboratory conditions (temperature: 22° ± 2°C, humidity: 50 ± 10%, and 12-hour light/dark cycles) and provided with ad libitum access to food and water. All animal experimental protocols, including procedures for pain management, surgical techniques, and humane euthanasia, were reviewed and approved by the Institutional Animal Care and Use Committee (IACUC) of Guangxi University (approval nos. GXU-2024-138 and GXU-2025-194). All surgical procedures were performed under sterile conditions. Rabbits were anesthetized via intramuscular injection of 0.4 ml of Shutaishen (tiletamine/

zolazepam combination anesthetic). After induction of anesthesia, the midnasal region (~3 cm by 4 cm) was shaved, cleaned with soap and water, disinfected with iodine solution, and sterilized with 75% ethanol. Local infiltration anesthesia was administered using 0.1 ml of 2% lidocaine hydrochloride injected along the nasal midline. A skin incision (~3 cm) was then made along the nasal midline to expose and carefully separate the left and right mucoperiosteum, revealing the anterior wall of the maxillary sinuses.

In the experimental group, the periosteum covering the anterior wall of the left maxillary sinus was carefully incised, and a sterile piece of biological hemostatic cotton was placed into the sinus cavity. Subsequently, 0.5 ml of *S. aureus* suspension (1×10^8 CFU/ml) was slowly injected into the sinus cavity, followed by meticulous suturing of the periosteum and skin incision. Three additional rabbits served as the blank control group, undergoing identical surgical procedures but without bacterial inoculation. Postoperative analgesia was provided through subcutaneous administration of buprenorphine (0.05 mg/kg) every 8 hours for 48 hours to minimize postoperative discomfort. Rabbits were closely monitored daily for signs of distress, infection, or complications. At the conclusion of the study, rabbits were humanely euthanized by first administering deep anesthesia through intramuscular injection of Shutaishen (tiletamine/zolazepam).

CBMRs' photocatalytic treatment of rabbit sinusitis under a magnetic field

First, the rabbit was anesthetized, and the treatment began after the rabbit's breathing was stable. All treatments were performed in a sterile environment. Half of a milliliter of CBMR solution (500 μg/ml) was injected into the rabbit sinuses. Optical fiber was introduced into rabbit sinuses, a Xe lamp (a 420-nm cutoff filter was installed to provide visible light) and a magnetic field were turned on, and treatment was performed for 1 hour. A robotic arm was used to manipulate the movement of the magnets, and the whole process was navigated and tracked with the aid of DR imaging. The wound was sutured at the end of the treatment, and blood samples were taken 3 days later for routine blood tests. After euthanizing rabbits, the sinus mucosa tissues were taken for histological analysis.

SEM analysis of sinus mucosa

After the rabbits were euthanized, the sinus mucosa was removed, rinsed with 0.1 M PBS buffer solution, and fixed in 10% formaldehyde solution for 12 hours. After fixation, the samples were washed three times with PBS buffer solution and then dehydrated with 30, 50, 70, 80, 90, 95, and 100% ethanol solution, respectively, for 15 min each. The dehydrated samples were freeze-dried overnight, and their surface morphology was observed by SEM.

Magnetic field simulation

COMSOL Multiphysics 6.1, commercial finite element software, was used to simulate the force of the swarm under the magnetic field. The liquid medium was water, and all walls are defined as nonslip boundaries. To simplify the calculation, we modeled the robot swarm as a disk with a diameter of 5 mm and a height of 500 μm. The specific equations are shown in the Supplementary Materials.

Statistical analysis

Data were analyzed using the statistical software program Prism 10.1 (GraphPad Software Inc., La Jolla, CA) and are presented as means. Student's *t* test was used to assess differences between two groups, and one-way or two-way analysis of variance (ANOVA) followed by Tukey's multiple comparisons test was applied to evaluate differences among multiple groups. Differences with $P < 0.05$ were considered statistically significant.

Supplementary Materials

The PDF file includes:

Legends for movies S1 to S5
Methods
Tables S1 and S2
Figs. S1 to S31

Other Supplementary Material for this manuscript includes the following:

Movies S1 to S5
MDAR Reproducibility Checklist

REFERENCES AND NOTES

1. Y. Hu, X. Ruan, X. Lv, Y. Xu, W. Wang, Y. Cai, M. Ding, H. Dong, J. Shao, D. Yang, X. Dong, Biofilm microenvironment-responsive nanoparticles for the treatment of bacterial infection. *Nano Today* **46**, 101602 (2022).
2. L. Dieltjens, K. Appermans, M. Lissens, B. Lories, W. Kim, E. V. Van der Eycken, K. R. Foster, H. P. Steenackers, Inhibiting bacterial cooperation is an evolutionarily robust anti-biofilm strategy. *Nat. Commun.* **11**, 107 (2020).
3. S. L. Chua, Y. Liu, J. K. H. Yam, Y. Chen, R. M. Vejborg, B. G. C. Tan, S. Kjelleberg, T. Tolker-Nielsen, M. Givskov, L. Yang, Dispersed cells represent a distinct stage in the transition from bacterial biofilm to planktonic lifestyles. *Nat. Commun.* **5**, 4462 (2014).
4. R. W. Bergmark, M. Pynnonen, Diagnosis and first-line treatment of chronic sinusitis. *JAMA* **318**, 2344–2345 (2017).
5. C. Bachert, L. Mannent, R. M. Naclerio, J. Mullol, B. J. Ferguson, P. Gevaert, P. Hellings, L. Jiao, L. Wang, R. R. Evans, G. Pirozzi, N. M. Graham, B. Swanson, J. D. Hamilton, A. Radin, N. A. Gandhi, N. Stahl, G. D. Yancopoulos, E. R. Sutherland, Effect of subcutaneous dupilumab on nasal polyp burden in patients with chronic sinusitis and nasal polyposis a randomized clinical trial. *JAMA* **315**, 469–479 (2016).
6. M. F. Mafee, B. H. Tran, A. R. Chapa, Imaging of rhinosinusitis and its complications: Plain film, CT, and MRI. *Clin. Rev. Allergy Immunol.* **30**, 165–185 (2006).
7. J. Meng, Y. Xiao, S. Gao, Antibiotics for acute sinusitis in children. *JAMA* **330**, 1909–1910 (2023).
8. Z. Huang, C. Chun, X. Li, Kidney targeting peptide-modified biomimetic nanoplatforms for treatment of acute kidney injury. *J. Control. Release* **358**, 368–381 (2023).
9. B. Wang, S. Handschuh-Wang, J. Shen, X. Zhou, Z. Guo, W. Liu, M. Pumera, L. Zhang, Small-scale robotics with tailored wettability. *Adv. Mater.* **35**, e2205732 (2023).
10. V. Milosavljevic, L. Kosaristanova, K. Dolezelikova, V. Adam, M. Pumera, Microrobots with antimicrobial peptide nanoarchitectonics for the eradication of antibiotic-resistant biofilms. *Adv. Funct. Mater.* **32**, 2112935 (2022).
11. G. Hwang, A. J. Paula, E. E. Hunter, Y. Liu, A. Babeer, B. Karabucak, K. Stebe, V. Kumar, E. Steager, H. Koo, Catalytic antimicrobial robots for biofilm eradication. *Sci. Robot.* **4**, eaaw2388 (2019).
12. I. Gorpynchenko, K. Nurimanov, T. Poroshina, V. Savchenko, G. N. Drannik, L. Dubuske, Microscopic assessment of prostate secretions in inflammatory versus non-inflammatory chronic pelvic pain syndrome in men. *J. Allergy Clin. Immunol.* **141**, AB124-AB124 (2018).
13. O. Felfoul, M. Mohammadi, S. Taherkhani, D. de Lanauze, Y. Z. Xu, D. Loghin, S. Essa, S. Jancik, D. Houle, M. Lafleur, L. Gaboury, M. Tabrizian, N. Kaou, M. Atkin, V. Te, G. Batist, N. Beauchemin, D. Radzioch, S. Martel, Magneto-aerotactic bacteria deliver drug-containing nanoliposomes to tumour hypoxic regions. *Nat. Nanotechnol.* **11**, 941–947 (2016).
14. X. Tang, Y. Yang, M. Zheng, T. Yin, G. Huang, Z. Lai, B. Zhang, Z. Chen, T. Xu, T. Ma, H. Pan, L. Cai, Magnetic-acoustic sequentially actuated CAR T cell microrobots for precision navigation and in situ antitumor immunoactivation. *Adv. Mater.* **35**, 202211509 (2023).
15. T. Gwisai, N. Mirkhani, M. G. Christiansen, T. T. Nguyen, V. Ling, S. Schuerle, Magnetic torque-driven living microrobots for increased tumor infiltration. *Sci. Robot.* **7**, eabo0665 (2022).
16. Y.-X. Zhu, H.-R. Jia, Y.-W. Jiang, Y. Guo, Q.-Y. Duan, K.-F. Xu, B.-H. Shan, X. Liu, X. Chen, F.-G. Wu, A red blood cell-derived bionic microrobot capable of hierarchically adapting to five critical stages in systemic drug delivery. *Exploration* **4**, 20230105 (2024).
17. Z. Wu, J. Troll, H.-H. Jeong, Q. Wei, M. Stang, F. Ziemssen, Z. Wang, M. Dong, S. Schnichels, T. Qiu, P. Fischer, A swarm of slippery micropropellers penetrates the vitreous body of the eye. *Sci. Adv.* **4**, eaat4388 (2018).

18. B. Zhang, H. Pan, Z. Chen, T. Yin, M. Zheng, L. Cai, Twin-bioengine self-adaptive micro/nanorobots using enzyme actuation and macrophage relay for gastrointestinal inflammation therapy. *Sci. Adv.* **9**, eadc8978 (2023).
19. Z.-H. Wang, M. Chu, N. Yin, W. Huang, W. Liu, Z. Zhang, J. Liu, J. Shi, Biological chemotaxis-guided self-thermophoretic nanoplatform augments colorectal cancer therapy through autonomous mucus penetration. *Sci. Adv.* **8**, eabn3917 (2022).
20. A. S. Chaudhary, A review of global initiatives to fight antibiotic resistance and recent antibiotics' discovery. *Acta Pharm. Sin. B* **6**, 552–556 (2016).
21. L. Ran, B. Lu, H. Qiu, G. Zhou, J. Jiang, E. Hu, F. Dai, G. Lan, Erythrocyte membrane-camouflaged nanoworms with on-demand antibiotic release for eradicating biofilms using near-infrared irradiation. *Bioact. Mater.* **6**, 2956–2968 (2021).
22. Y. Zhao, Y. Yu, F. Gao, Z. Wang, W. Ch, C. Ch, J. Yang, Y. Yao, J. Du, C. Zhao, Y. Wu, A highly accessible copper single-atom catalyst for wound antibacterial application. *Nano Res.* **14**, 4808–4813 (2021).
23. Y. Xing, J. Xiu, M. Zhou, T. Xu, M. Zhang, H. Li, X. Li, X. Du, T. Ma, X. Zhang, Copper single-atom jellyfish-like nanomotors for enhanced tumor penetration and nanocatalytic therapy. *ACS Nano* **17**, 6789–6799 (2023).
24. X. Fan, Y. Gao, F. Yang, J. L. Low, L. Wang, B. Paulus, Y. Wang, A. Trampuz, C. Cheng, R. Haag, A copper single-atom cascade bionanocatalyst for treating multidrug-resistant bacterial diabetic ulcer. *Adv. Funct. Mater.* **33**, 2301986 (2023).
25. J. Xiong, H.-Y. Zeng, S. Xu, J.-F. Peng, F.-Y. Liu, L.-H. Wang, Enhancing the intrinsic properties of flower-like BiOI by S-doping toward excellent photocatalytic performances. *J. Mater. Sci. Technol.* **118**, 181–189 (2022).
26. Y. Shen, C. Ren, L. Zheng, X. Xu, R. Long, W. Zhang, Y. Zhou, Y. Zhang, Y. Yao, H. Chi, J. Wang, Q. Shen, Y. Xiong, Z. Zou, Y. Zhou, Room-temperature photosynthesis of propane from CO_2 with Cu single atoms on vacancy-rich TiO_2. *Nat. Commun.* **14**, 1117 (2023).
27. C. E. Garcia-Vargas, G. Collinge, D. Yun, M.-S. Lee, V. Muravev, Y.-Q. Su, X. I. Pereira-Hernandez, D. Jiang, V.-A. Glezakou, E. J. M. Hensen, R. Rousseau, A. K. Datye, Y. Wang, Activation of lattice and adatom oxygen by highly stable ceria- supported Cu single atoms. *ACS Catal.* **12**, 13649–13662 (2022).
28. K. Chen, D. Ma, Y. Zhang, F. Wang, X. Yang, X. Wang, H. Zhang, X. Liu, Urea electrosynthesis from nitrate and CO_2 on diatomic alloys. *Adv. Mater.* **36**, 202402160 (2024).
29. Y. Cai, J. Fu, Y. Zhou, Y.-C. Chang, Q. Min, J.-J. Zhu, Y. Lin, W. Zhu, Insights on forming N,O-coordinated Cu single-atom catalysts for electrochemical reduction CO_2 to methane. *Nat. Commun.* **12**, 586 (2021).
30. J. Yu, B. Wang, X. Du, Q. Wang, L. Zhang, Ultra-extensible ribbon-like magnetic microswarm. *Nat. Commun.* **9**, 3260 (2018).
31. J. Yu, D. Jin, K.-F. Chan, Q. Wang, K. Yuan, L. Zhang, Active generation and magnetic actuation of microrobotic swarms in bio-fluids. *Nat. Commun.* **10**, 5631 (2019).
32. B. Wang, D. Liu, Y. Liao, Y. Huang, M. Ni, M. Wang, Z. Ma, Z. Wu, Y. Lu, Spatiotemporally actuated hydrogel by magnetic swarm nanorobotics. *ACS Nano* **16**, 20985–21001 (2022).
33. M. Sun, K. F. Chan, Z. Zhang, L. Wang, Q. Wang, S. Yang, S. M. Chan, P. W. Y. Chiu, J. J. Y. Sung, L. Zhang, Magnetic microswarm and fluoroscopy-guided platform for biofilm eradication in biliary stents. *Adv. Mater.* **34**, e2201888 (2022).
34. L. Wang, D. Zheng, P. Harker, A. B. Patel, C. F. Guo, X. Zhao, Evolutionary design of magnetic soft continuum robots. *Proc. Natl. Acad. Sci. U.S.A.* **118**, (2021).
35. H. Yu, M. Wang, J. Yan, H. Dang, H. Zhu, Y. Liu, M. Wen, G. Li, L. Wu, Complete mineralization of phenolic compounds in visible-light-driven photocatalytic ozonation with single-crystal WO_3 nanosheets: Performance and mechanism investigation. *J. Hazard. Mater.* **433**, 128811 (2022).
36. H. Zhang, L. Meng, Y. Zhang, Q. Xin, Y. Zhou, Z. Ma, L. Zuo, C. Zheng, J. Luo, Y. Zhou, C. Ding, J. Li, Light and magnetism orchestrating aquatic pollutant-degradation robots in programmable trajectories. *Adv. Mater.* **36**, e2311446 (2024).
37. C. C. Mayorga-Martinez, J. Zelenka, K. Klima, P. Mayorga-Burrezo, L. Hoang, T. Ruml, M. Pumera, Swarming magnetic photoactive microrobots for dental implant biofilm eradication. *ACS Nano* **16**, 8694–8703 (2022).
38. S. Schuerle, A. P. Soleimany, T. Yeh, G. M. Anand, M. Haberli, H. E. Fleming, N. Mirkhani, F. Qiu, S. Hauert, X. Wang, B. J. Nelson, S. N. Bhatia, Synthetic and living micropropellers for convection-enhanced nanoparticle transport. *Sci. Adv.* **5**, eaav4803 (2019).
39. M. Chen, Y. Cai, G. Li, H. Zhao, T. An, The stress response mechanisms of biofilm formation under sub-lethal photocatalysis. *Appl. Catal. B Environ.* **307**, 121200 (2022).
40. E. R. Wald, *Staphylococcus aureus*: Is it a pathogen of acute bacterial sinusitis in children and adults? *Clin. Infect. Dis.* **54**, 826–831 (2012).
41. D. Singhal, A. Jekle, D. Debabov, L. Wang, B. Khosrovi, M. Anderson, A. Foreman, P.-J. Wormald, Efficacy of NVC-422 against *Staphylococcus aureus* biofilms in a sheep biofilm model of sinusitis. *Int. Forum Allergy Rhinol.* **2**, 309–315 (2012).
42. H. Zhang, Z. Li, C. Gao, X. Fan, Y. Pang, T. Li, Z. Wu, H. Xie, Q. He, Dual-responsive biohybrid neutrobots for active target delivery. *Sci. Robot.* **6**, eaaz9519 (2021).
43. C. Gao, Y. Wang, Z. Ye, Z. Lin, X. Ma, Q. He, Biomedical micro-/nanomotors: From overcoming biological barriers to in vivo imaging. *Adv. Mater.* **33**, 202000512 (2021).
44. D. Walker, B. T. Kaesdorf, H.-H. Jeong, O. Lieleg, P. Fischer, Enzymatically active biomimetic micropropellers for the penetration of mucin gels. *Sci. Adv.* **1**, e150050 (2015).
45. X. Wu, Y. Zhang, X. Chen, J. Chen, M. Jia, Inflammatory immune response in rabbits with *Staphylococcus aureus* biofilm-associated sinusitis. *Int. Forum Allergy Rhinol.* **8**, 1226–1232 (2018).
46. M. Jia, Z. Chen, Y. Guo, X. Chen, X. Zhao, Efficacy of silk fibroin-nano silver against *Staphylococcus aureus* biofilms in a rabbit model of sinusitis. *Int. J. Nanomedicine* **12**, 2933–2939 (2017).
47. P. K. Verma, Advancement in photocatalytic acceptorless dehydrogenation reactions: Opportunity and challenges for sustainable catalysis. *Coord. Chem. Rev.* **472**, 214805 (2022).
48. X. Bian, Y. Zhao, C. Zhou, T. Zhang, Minimizing temperature bias through reliable temperature determination in gas-solid photothermal catalytic reactions. *Angew. Chem. Int. Ed. Engl.* **62**, 202219340 (2023).
49. L. Yang, J. Jiang, X. Gao, Q. Wang, Q. Dou, L. Zhang, Autonomous environment-adaptive microrobot swarm navigation enabled by deep learning-based real-time distribution planning. *Nat. Mach. Intell.* **4**, 480–493 (2022).
50. L. Xie, X. Pang, X. Yan, Q. Dai, H. Lin, J. Ye, Y. Cheng, Q. Zhao, X. Ma, X. Zhang, G. Liu, X. Chen, Photoacoustic imaging-trackable magnetic microswimmers for pathogenic bacterial infection treatment. *ACS Nano* **14**, 2880–2893 (2020).
51. F. Lamoth, K. Prakash, C. Beigelman-Aubry, J. W. Baddley, Lung and sinus fungal infection imaging in immunocompromised patients. *Clin. Microbiol. Infect.* **30**, 296–305 (2024).
52. Y. Zhang, Y. Zhang, W. Liu, G. Wei, Q. Liu, G. Shao, X. Gu, X. Cui, Z. Zhou, Y. Wang, S. Zhao, F. Muhammad, S. Li, T. Li, Y. Du, Bioinspired nanozymes as nanodecoys for urinary tract infection treatment. *ACS Nano* **18**, 9019–9030 (2024).
53. P. Mayorga-Burrezo, C. C. Mayorga-Martinez, J. Kim, M. Pumera, Hybrid magneto-photocatalytic microrobots for sunscreens pollutants decontamination. *Chem. Eng. J.* **446**, 137139 (2022).

Acknowledgments: We thank Q. Wang for assistance on the swarm's motion validation.
Funding: This work was supported by the National Natural Science Foundation of China (nos. 52175550, 52475308, and 524B2073), Key Program of the National Natural Science Foundation of Guangxi (no. 2025GXUNSFDA069003), Specific Research Project of Guangxi for Research Bases and Talents (no. 2022AC21200), Innovation Project of Guangxi Graduate Education (YCBZ2024042), the Special Fund for Science and Technology Development of Guangxi (No. AD25069078), Shenzhen Medical Research Fund (SMRF A2303074), Natural Science Foundation of Shenzhen Science and Technology Commission with grant no. RCBS20200714114920190, Guangdong Basic and Applied Basic Research Foundation (2021A1515010672), the Bagui Youth Talents project of Guangxi Zhuang Autonomous Region, Research Fellow Scheme (project no. RFS2122-4S03), and Strategic Topics Grant (project no. STG1/E-401/23-N) from the Hong Kong Research Grants Council (RGC). The authors also acknowledge support from the SIAT-CUHK Joint Laboratory of Robotics and Intelligent Systems and the Multi-Scale Medical Robotics Center (MRC), InnoHK, at the Hong Kong Science Park. The simulated software involved in this manuscript is supported by the high-performance computing platform of Guangxi University. **Author contributions:** H.Y.: Writing—original draft, data curation, conceptualization, validation, visualization, and methodology. Xurui Liu: Writing—review and editing, validation, visualization, and investigation. Y.Z.: Writing—review and editing, project administration, conceptualization, investigation, funding acquisition, and supervision. J.S.: Supervision and in vivo experiment. Xijun Liu: Project administration and material preparation experiment. S.L,: In vivo experiment and project administration. X.W.: Particle motion verification experiment and project administration. B.S.: Writing and editing. H.D.: Writing and editing. L.X.: Writing and editing. B.Z.: Writing and editing and funding acquisition. J.D.: Writing and editing. Q.X.: Writing and editing. L.Z.: Writing and editing, discussion, and supervision. B.W.: Writing—review and editing, project administration, investigation, funding acquisition, and supervision.
Competing interests: Y.Z., H.Y., and B.Z. are inventors on an authorized patent related to this work filed by the China National Intellectual Property Administration (no. ZL 202310895675.6, published 3 May 2024). The authors declare that they have no other competing interests.
Data and materials availability: All data needed to support the conclusions of this manuscript are included in the main text or Supplementary Materials or accessible via Zenodo: https://zenodo.org/records/15486143.

Submitted 11 September 2024
Accepted 29 May 2025
Published 25 June 2025
10.1126/scirobotics.adt0720

Science Robotics

Photocatalytic microrobots for treating bacterial infections deep within sinuses

Haidong Yu, Xurui Liu, Yabin Zhang, Jie Shen, Xijun Liu, Shubo Liu, Xiangyu Wang, Bonan Sun, Huihui Du, Lin Xu, Bingsuo Zou, Jianning Ding, Qingsong Xu, Li Zhang, and Ben Wang

Sci. Robot. **10** (103), eadt0720. DOI: 10.1126/scirobotics.adt0720

Science Robotics (ISSN 2470-9476) is published by the American Association for the Advancement of Science. 1200 New York Avenue NW, Washington, DC 20005. The title *Science Robotics* is a registered trademark of AAAS.